

A DEEP *CHANDRA* LOOK AT THE LOW L_B ELLIPTICAL NGC 821: NOT ONLY WIND AND X-RAY BINARIES

S. PELLEGRINI¹, A. BALDI², D.W. KIM², G. FABBIANO², R. SORIA^{2,3}, A. SIEMIGINOWSKA²,
M. ELVIS²

¹ Astronomy Department, Bologna University, Italy; silvia.pellegrini@unibo.it

² Harvard-Smithsonian Center for Astrophysics, 60 Garden St, Cambridge, MA 02138

³ Mullard Space Science Laboratory, University College London, Holmbury St Mary, UK

Submitted to *ApJ*

ABSTRACT

The nearby, low L_B elliptical galaxy NGC821, known to host a central massive black hole but inactive at all wavelengths, has been observed with deep *Chandra* pointings, for a total exposure of 230 ksec, in order to search for nuclear emission and gas available for accretion. Within its optical image, 41 X-ray sources are detected, with spectral properties typical of low mass X-ray binaries (LMXBs); their X-ray luminosity function (XLF) was derived down to a 0.3–8 keV luminosity of 3×10^{37} erg s⁻¹. At the position of the galactic center a source of $L(0.3\text{--}8\text{ keV}) = 6 \times 10^{38}$ erg s⁻¹ is detected for the first time, even though extended. Its spectral shape is quite hard ($\Gamma = 1.49_{-0.13}^{+0.14}$), without intrinsic absorption. This source is surrounded by three other sources with a spectral shape typical of LMXBs and luminosities on the brightest end of the XLF. Only one is consistent with being pointlike, the other two could be the superposition of few point sources and/or truly diffuse emission; in particular, one of them resembles a jet-like feature. Diffuse emission is detected out to a radius of $\sim 30''$. However, different lines of investigation consistently provide no evidence for hot gas, either close to the center or on a larger scale. The diffuse emission instead comes mostly from unresolved LMXBs, with a possible minor contribution from other types of stellar sources. Hydrodynamical simulations specific for NGC 821 show that the hot gas is driven out of the galaxy in a wind sustained by type Ia supernovae, but also that it is accreting towards the center from within a very small inner region. The total amount of gas accreted in this way during the galaxy's lifetime, though, is just few percent of the central black hole mass. A companion paper (Pellegrini et al. 2006) presents further observational results obtained with *Spitzer* and the VLA, and discusses possible accretion modalities for this central massive black hole.

Subject headings: galaxies: elliptical and lenticular, CD – galaxies: individual: NGC 821 – galaxies: nuclei – X-rays: galaxies – X-rays: ISM

1. INTRODUCTION

NGC 821 is an isolated elliptical galaxy at a distance of 24.1 Mpc (Smith et al. 2004; see Table 1), with very regular optical isophotes of disk shape (Bender et al. 1994, Lauer et al. 2005) and an old and metal rich stellar population as typical of elliptical galaxies (Proctor et al. 2005). No cold (HI) or dusty ISM has been revealed in it (Lauer et al. 2005, Sarzi et al. 2006). NGC 821 is also one of those ~ 30 nearby galactic spheroids for which a central supermassive black hole (MBH) has been claimed based on resolved dynamical studies (Ferrarese & Ford 2005). The mass of this MBH is $8.5 \times 10^7 M_\odot$ (Table 1) and its Eddington luminosity is $L_{Edd} \sim 1.1 \times 10^{46}$ erg s⁻¹. However, this MBH is extremely quiescent at all wavelengths (see also Pellegrini et al. 2006), and represents an excellent example of the class of "inactive" nuclei, that are very common in the local universe (e.g., Pellegrini 2005a, Ho 2005) and key to our understanding of the mechanisms of AGN evolution and nuclear feedback, that have been fundamental for shaping our universe (e.g., Springel, Di Matteo & Hernquist 2005). Since it is nearby, NGC821 is a prime target for observing a quiescent nucleus and its surroundings.

These considerations motivated our first study of NGC821 in X-rays with *Chandra* (Fabbiano et al. 2004,

hereafter F04). X-ray emission is a key symptom of nuclear activity resulting from accretion onto a MBH (Rees 1984), and the hot ISM that could provide a source of fuel is readily visible in the X-rays (e.g., Fabian & Canizares 1988; Loewenstein et al. 2001; Pellegrini 2005a). Previous observations of NGC821 with the *ROSAT* PSPC had placed an upper limit of 2.8×10^{40} erg s⁻¹ (O'Sullivan et al. 2001) on the total X-ray luminosity, suggesting a low content of hot gas (e.g., Kim et al. 1992). However, only with the sub-arcsecond resolution of *Chandra* could we attempt to resolve the different components of the X-ray emission (hot gas, nucleus, population of low mass X-ray binaries - LMXBs). The shallow (39 ks) *Chandra* observation, performed in 2002, revealed diffuse emission in the central galactic region, possibly from a hot interstellar medium. We did not detect any source that could be unequivocally identified as the galactic nucleus (for which we derived $L_X/L_{Edd} < 10^{-7}$), but an intriguing S-shaped feature crossing the center of the galaxy was observed. Explanations for this feature included either a weak two-sided X-ray nuclear jet, or a hot gas filament, at a temperature higher than that of the surrounding gas. This opened the possibilities that the accretion power could end mostly into mechanical rather than radiative power (Di Matteo et al. 2003, Pellegrini et al. 2003a, Fabbiano et al. 2003), or that the accretion flow may

be disrupted by nuclear feedback (e.g., Ciotti & Ostriker 2001, Omma et al. 2004; see also Soria et al. 2006a,b).

In this paper we report the results of the analysis of deep *Chandra* observations (for a total exposure of nearly 230 ks) aimed at better defining the properties of the various sources in the central galactic region. With the deep *Chandra* exposure, we can constrain all the components (nucleus, hot gas, unresolved sources) contributing to the emission, a necessary and critical step when the goal is to understand the accretion process. For example, we can detect a significant portion of the LMXB population, which was barely visible in the 2002 data, and thanks to the calculation of its X-ray Luminosity Function (XLF) we can now discriminate between the contributions to the diffuse emission of the unresolved LMXBs and of the hot ISM (e.g., Kim & Fabbiano 2004). Moreover, determining the properties of the hot ISM also gives clues on the way the ISM evolves in this galaxy, and more in general in galaxies of similar optical luminosity (e.g., Pellegrini & Ciotti 1998, Sansom et al. 2006, David et al. 2006). A companion paper (Pellegrini et al. 2006) presents an observational campaign aimed at determining the properties of the nuclear emission of NGC 821 at various wavelengths, including more sensitive proprietary VLA and *Spitzer* IRAC observations, together with archival *HST* observations.

The paper is organized as follows: in Section 2 we describe the *Chandra* observations and data preparation; in Sections 3, 4 and 5 we report the results of the X-ray analysis, respectively for the LMXB population, the nuclear region, and the diffuse emission; in Section 6 we discuss the implications of our observations; in Section 7 we summarize our results.

2. CHANDRA OBSERVATIONS AND DATA PREPARATION

NGC 821 was observed with *Chandra* ACIS-S (Weiskopf et al. 2000) seven times between November 2002 and June 2005, for a total exposure of 230 ks (Table 2). Here we consider both the archival observations (ObsID 4408 and 4006 in Tab. 2), already presented in F04, and the new unpublished data obtained in 2004 and 2005.

The satellite telemetry is processed at the *Chandra* X-ray Center (CXC) with the Standard Data Processing (SDP) pipelines, to correct for the motion of the satellite and to apply instrument calibration. The data used in this work were reprocessed in custom mode with the version 7.6.0 of the SDP, to take advantage of improvements in processing software and calibration, not available at the time of the original processing. Verification of the data products showed no anomalies. The relative astrometry of the different observations was corrected by using detected sources (above a 3σ threshold) as reference points (<http://cxc.harvard.edu/cal/ASPECT/align evt/>).

The data products were then analyzed with the CXC CIAO v3.0.1 software and the HEASARC XSPEC package. CIAO Data Model tools were used for data processing, such as screening out bad pixels and producing images in given energy bands. Calibration files in CALDB version 3.1.0 of June 2005 were used. The data were screened to exclude two "hot" columns in the ACIS-S3 CCD at chip-x columns 512 and 513 (at the b and c node boundaries). No significant background flares were observed in these data, so no further screening was nec-

essary. A time-dependent gain correction (Vikhlinin et al. 2003) was applied to the SDP Level 2 event files of the first two observations before further analysis. This correction was already included in the SDP Level 2 event files of the other observations supplied by the CXC. The seven observations were then coadded to produce a deep image, using the CIAO task *merge_all*, which takes as input the event files and the relative aspect solution (ASOL) files, and reprojects the coordinates of all the observations onto the first one.

Below we report the results of the analysis of these data.

3. THE LOW MASS X-RAY BINARIES POPULATION

Figure 1 shows the merged X-ray image, with the D25 ellipse of NGC821 overplotted (this ellipse is the isophote of the 25.0 B-mag/square arcsec brightness level, Tab. 1); also marked are the X-ray sources detected by the CIAO task *wavdetect*. Of the 104 sources detected within the ACIS-S3 CCD, 41 lie inside the D25 ellipse. Excluding minor contamination from interlopers (see Sect. 3.1 and 5.6), these sources represent the LMXBs population of NGC821 (see Fabbiano 2006 for a review on X-ray binary populations of galaxies). The range of net detected counts for the sources within D25 is 8–300 counts, corresponding to 0.3–8 keV luminosities of $2 \times 10^{37} - 8 \times 10^{38} \text{ erg s}^{-1}$, when using the energy conversion factor described in Sect. 3.1 below.

X-ray colors were calculated for these sources, following the prescription of Kim et al. (2004), who define colors as $C21 = -\log M + \log L$, and $C32 = -\log H + \log M$, where L, M, and H are the counts detected respectively in the energy bands 0.3–0.9 keV, 0.9–2.5 keV and 2.5–8 keV. These counts were corrected for the temporal QE variation, referring them all to the first observing epoch (Nov. 2002, Tab. 2), and for the effect of the Galactic absorption (using the value in Table 1). Figure 2 shows the $C32 - C21$ distribution; the grid gives the location of spectra described by power laws with given values of the photon index Γ and intrinsic column density N_H . In agreement with previous spectral studies of LMXB populations (e.g., Kim, Fabbiano & Trinchieri 1992; Irwin, Athey & Bregman 2003), most well-defined colors fall near a typical $\Gamma = 1.5 - 2.0$ spectrum, with no intrinsic absorption.

3.1. The LMXB X-ray Luminosity Function

For the point sources falling within the D25 ellipse we estimated an XLF, that in differential form can be expressed as:

$$\frac{dN}{dL_X} = k \left(\frac{L_X}{10^{38} \text{ erg s}^{-1}} \right)^{-\beta}. \quad (1)$$

To construct the XLF, we calculated fluxes and luminosities of the point sources in the 0.3–8 keV band with an energy conversion factor (ECF) corresponding to an assumed power law spectral shape with $\Gamma = 1.7$ and Galactic N_H (see Fig. 2 for a justification of this assumption). As done for the colors, we took into account the temporal QE variation by calculating the ECF in each observation and then taking an exposure-weighted mean ECF. The ECF over the 0.3–8 keV band varied by $\sim 2.5\%$ between 2002 and 2005. We then corrected the XLF to eliminate

biases and incompleteness effects, which could affect the lowest luminosity range, causing an artificial break (Kim & Fabbiano 2003, 2004; Kim et al. 2006). We simulated $\sim 20,000$ point sources, added them one by one to the observed image, and then run *wavdetect* to determine whether the added source was detected. With this procedure we correct simultaneously for incompleteness near the detection threshold, Eddington bias (Eddington 1913) and source confusion. In the simulations, we assumed a typical XLF of differential slope of $\beta = 2$; however, the adopted slope does not affect the results significantly, and neither does the assumed radial distribution of point sources (which we assume to follow the optical light, as observed in many elliptical galaxies, see Fabbiano 2006). We excluded 11 sources at the center ($R < 10''$), because of the large photometric error caused by confusion with other overlapping sources, and by the possible presence of some diffuse emission; these conditions make the incompleteness corrections uncertain. With the above procedure, we established the 90% completeness limit (i.e., the luminosity at which 10% of sources would not be detected inside the D25 ellipse, excluding the central $10''$) to be $L_X = 3 \times 10^{37}$ erg s $^{-1}$ (or $F_X = 4.3 \times 10^{-16}$ erg cm $^{-2}$ s $^{-1}$) in the 0.3–8 keV band. We can reliably correct the XLF to a luminosity of $\sim 2/3$ of the 90% limit. The resulting cumulative XLF [i.e., the number of sources $N(> L_X)$] is shown in Fig. 3. From the log N – log S relation derived for the ChaMP plus CDF data (Kim, M. et al. 2006), we then estimated that the number of expected cosmic background sources (mostly AGN) falling within the D25 ellipse and brighter than the 90% completeness limit is 3, corresponding to a source contamination of 7%.

To establish the functional form of the XLF, we fitted the bias-corrected differential XLF [eq. (1)] with single power-laws, using both the Cash and χ^2 statistics in the CIAO *Sherpa* modeling and fitting application. We found that a single power-law represents well the XLF, with a best fit slope $\beta = 2.0 \pm 0.3$, compatible with other power-law fits of LMXB XLFs (Kim & Fabbiano 2004; Kim et al. 2006) and a best fit amplitude $k = 8.4_{-2.5}^{+3.1}$. Even without the correction for incompleteness, that is significant only at the point corresponding to the faintest fluxes ($L_X = 2 \times 10^{37}$ erg s $^{-1}$), a single power law is a good fit all the way down to $L_X = 3 \times 10^{37}$ erg s $^{-1}$. Figure 3 may suggest a low luminosity break around $L_X \sim 5 \times 10^{37}$ erg s $^{-1}$. This break was suggested to be a universal feature of LMXB populations (Gilfanov 2004), but is not observed in all cases (Kim et al. 2006). For NGC821 there is no compelling evidence for such a break, given the size of the error bars, and the good fit with a single power-law model. The combined LMXB XLF (Kim & Fabbiano 2004; Gilfanov 2004) shows a high luminosity break at $L_X > (5.0 \pm 1.6) \times 10^{38}$ erg s $^{-1}$, that may originate from the presence of neutron star and black hole binary populations. We cannot constrain here the high luminosity shape of the XLF because of the small number of luminous sources (only 2 sources have $L_X > 5 \times 10^{38}$ erg s $^{-1}$).

In contrast to the uniform slope, the amplitude of the XLF varies widely from galaxy to galaxy, reflecting the varying content of LMXBs per unit galactic luminosity. For their sample of early type galaxies, from integration

of the XLF above $L_{X,min} = 10^{37}$ erg s $^{-1}$, Kim & Fabbiano (2004) estimate the total L_X due to LMXBs and the average ratio $L_X/L_B = (0.9 \pm 0.5) \times 10^{30}$ erg s $^{-1} L_{B,\odot}^{-1}$. For NGC821 this ratio is 0.4×10^{30} erg s $^{-1} L_{B,\odot}^{-1}$, lower than the mean value by 1σ . This ratio is known to correlate with the total specific frequency of globular clusters, but this quantity unfortunately is not available for NGC821. Based on the L_X/L_B ratio, we would expect NGC821 to have a relatively poor globular cluster population.

4. THE CENTRAL REGION OF NGC821 – RESOLVED SOURCES

Figure 4 shows the central region of the image obtained from the merged data, in three spectral bands (0.3–1 keV, 1–2 keV and 2–4 keV) that cover the energy range where most of the counts are detected. From these three images in different spectral bands we also obtained an adaptively smoothed (using the CIAO task ‘csmooth’) color image (Fig. 5), where the data were smoothed using scales ranging from 1 to 20 pixels ($0''.5 - 10''$). Given the small extent of the region considered, no exposure correction was needed. Figure 5 shows diffuse emission at the center, that follows the optical shape of the galaxy: it is elongated in the NW-SE direction, roughly aligned with the optical major axis (see also Tab. 1, Fig. 1 and Fig. 7 below). Most of the diffuse emission is concentrated well within one R_e (that is $43''.9$, while the size of Fig. 5 is $55''$). Its color indicates emission mostly in the soft (red) and medium (green) energy bands. Harder emission from a few central point-like sources is also visible.

Below we concentrate on the X-ray analysis of the sources detected in the central region; in Sect. 5 we report the analysis of the diffuse emission, for the central region and the whole galaxy.

4.1. Detection and spatial properties

We can now establish with higher significance than in F04 the morphology of the central X-ray emission. In particular, F04 had identified three possibly connected extended central emission regions (that they called S1 through S3) and a point-like source to the north-east of this grouping (labelled NE source). *wavdetect* detects all these emission regions in the merged data, plus another source that we call S4 (Fig. 6). F04 had found the spatial distribution of photons of the S1–S3 sources to be more extended than expected for point-like sources seen through the *Chandra* mirrors, and suggested that they may be part of an S-shaped jet or filament, possibly connected with low-level or past nuclear activity. With the longer exposure, it is apparent (Fig. 6) that the emission of S3 may be point-like, suggesting that this source is a luminous LMXB, but the other sources are more extended.

In order to establish the spatial properties of S1–S4, following F04 we compared the spatial distribution of their counts with that of the on-axis image of the quasar GB 1508+5714, a hard point-like source (Siemiginowska et al. 2003). GB 1508+5714 gives a good representation of the *Chandra* ACIS-S PSF for our analysis, since it lies at the same distance from the aimpoint as S1–S4 and is similarly hard (see Sect. 4.3 below). The image

of GB 1508+5714 contains 5,300 counts within $2''$ of the centroid of the count distribution; the ratio of counts within the $1''$ – $2''$ annulus to those in the central circle of $1''$ radius is $Ratio(PSF)=0.043\pm 0.001$ (1σ). The isolated NE source in this central field (Fig. 6) has a total of 173 source counts and $Ratio(NE)=0.123\pm 0.083$, a value consistent with that of our reference quasar, within the 1σ error.

The total number of source counts for S1–S4 are 184, 250, 326 and 84 respectively; the analogous ratios for the background-subtracted counts, around the centroids determined by *wavdetect*, are $Ratio(S1)=0.59\pm 0.11$, $Ratio(S2)=0.77\pm 0.10$, $Ratio(S3)=0.20\pm 0.06$, and $Ratio(S4)=0.80\pm 0.15$. Therefore the spatial distribution of the counts from S1–S4 is extended, when we compare it with that of the quasar. If, more conservatively, we use as a benchmark the NE source, we find that S3 is point-like, while S1, S2 and S4 are all significantly more extended than the NE source (at 3.5 , 4.6 and 4σ respectively). Although the significance of the NE source is such that its *Ratio* is less well determined than that of the quasar, this source would be affected by similar small amounts of smearing in the merging process as the S1–S4 sources. [Note that in F04 the NE source had a $Ratio(NE)=0.057\pm 0.054$, consistent within the errors with the value we find in this paper, although the nominal value is smaller; this justifies using NE as a benchmark.]

In conclusion, excluding source S3, the counts of S1, S2 and S4 cannot come entirely from a point source. While the previous *Chandra* observation was suggestive of a central emission feature intrinsically elongated, possibly mostly due to diffuse emission (F04), the present imaging analysis suggests a cluster of extended sources. With these data it remains possible that each source is truly extended or produced by several point-like components, or alternatively due to a point-like component embedded in truly diffuse emission.

4.2. Position of the nucleus - S2

From the Two Micron All Sky Survey (2MASS, Skrutskie et al. 2006), the center of NGC821 is at RA= $02^h 08^m 21^s.14$, Dec= $+10^\circ 59' 41''.7$ (J2000), with an uncertainty of $1''.25$ (at 95% confidence), as reported in the NASA/IPAC Extragalactic Database (NED). Considering the *Chandra* aspect uncertainty (the 90% uncertainty circle has a radius of $\lesssim 0''.6$), this position agrees with that of the extended source S2 determined by *wavdetect*, that is RA= $02^h 08^m 21^s.10$, Dec= $+10^\circ 59' 41''.6$, with an offset of just $0''.6$.

In addition, we compared the *Chandra* and *HST* positions, by using archival WFPC2 F555W and F814W filter images. We improved the astrometry of the WFPC2 images, re-fitting the coordinate grid to all sources with positional errors $\lesssim 0''.3$ in the 2MASS All-Sky Catalog of Point Sources (Cutri et al. 2003) and the USNO-B1.0 Catalog (Monet et al. 2003). A comparison of the recalibrated WFPC2 images, now astrometrically-corrected to an accuracy of $\sim 0''.2$, with the *Chandra* image identifies seven sources with optical/X-ray coincidences, not including the nuclear source S2 (Fig. 7). Six of them are inside the D25 ellipse, the seventh source is outside and more likely to be a background quasar (the six inner sources are marked with yellow circles in Figure 7).

There is no systematic shift or rotation between the revised *HST* and *Chandra* positions. For each of the seven sources the displacement between the optical and X-ray positions is $< 0''.6$; the root-mean-square displacement for the whole sample is $\sigma = 0''.26$, consistent with the expected random scatter. In the recalibrated WFPC2 image, now the most accurate reference for deriving positions, the nucleus is located at RA= $02^h 08^m 21^s.13$, Dec= $+10^\circ 59' 41''.8$ (i.e., within $0''.2$ of the 2MASS position). In conclusion, the *wavdetect* center of S2 is $0''.5$ off the recalibrated WFPC2 optical nucleus (Fig. 8), a distance within the *Chandra* uncertainty.

4.3. Spectral analysis of sources S1–S4

We extracted the spectra of sources S1–S4 from the merged event file, using the extraction regions shown in Fig. 6; the background spectrum was derived from a source-free region outside the optical body of the galaxy but still inside the ACIS-S3 chip. We also generated instrumental response files, weighted by the exposure time of each individual observation. Prior to fitting, we binned the spectra in order to have at least 20 total counts per energy bin, with the exception of the weakest source (S4) that was rebinned at 10 counts per energy bin¹. We then fitted the spectra with an absorbed power-law model [XSPEC model: *wabs(powerlaw)*] and an optically thin thermal model corrected for absorption [XSPEC model: *wabs(apec)*, with abundance $Z=0.5$ in solar units, and the solar abundance values of Anders & Grevesse 1989]; the absorption was let to be a free parameter. The low number of counts did not allow for fits with composite spectral models. The results are summarized in Table 3.

The spectral analysis indicates a hard spectral shape (thermal emission of $kT \gtrsim 3$ keV or power law emission with $\Gamma = 1.4 - 2.3$), with little or no intrinsic absorption. The resulting column densities N_H are consistent with the Galactic value ($6.2 \times 10^{20} \text{ cm}^{-2}$) for most of the fits in Table 3; if N_H is fixed to be Galactic, the best fit spectral parameters are substantially unchanged within the uncertainties. The spectral properties of S1–S4 are overall consistent with those typical of LMXBs (see, e.g., Sect. 3), even though these sources look extended (Sect. 4.1). The source at the nucleus (S2) seems to be harder than the other sources.

Table 3 lists the source luminosities calculated from the best fit parameters. S2 has a luminosity of about $6 \times 10^{38} \text{ erg s}^{-1}$; since it is extended, a nuclear point source, if contributes to the emission of S2, will have a smaller luminosity. Since we have now established that S2 is coincident with the nucleus (Sect. 4.2), it is reasonable that a fraction of the S2 emission originates from the MBH. However, an estimate of this fraction would not be unique, because it will require some model assumptions (e.g., one could model S2 as a point source plus some extended emission in various ways). F04 derived a 3σ upper limit for the nuclear luminosity of $L_X < 4.6 \times 10^{38} \text{ erg s}^{-1}$ in the 0.3–10 keV band; they assumed that all of the detected emission in the central S-shaped feature (Sect. 4.1) was truly extended, and calculated the limit from the largest emission found in

¹ When grouping with different criteria, or using the Cash statistics instead of the χ^2 one, the spectral results for this source do not change significantly.

a $1'' \times 1''$ sliding cell moved across this feature. In order to avoid model dependent results, we adopt as upper limit to the MBH emission the value derived with the same procedure used in F04, with the $1'' \times 1''$ cell slid over and around S2. This gives a 3σ upper limit of $L_X < 2.8 \times 10^{38} \text{erg s}^{-1}$ in the 0.3–8 keV band, and $L_X < 1.8 \times 10^{38} \text{erg s}^{-1}$ in the 2–10 keV band.

5. THE DIFFUSE EMISSION AND THE HOT ISM CONTRIBUTION

Estimating the amount of gaseous emission in NGC821 is important, because this hot gas could be a source of fuel for the nuclear MBH (see Sect. 1). The ACIS-S adaptively smoothed mapped color image of the NGC 821 field (Fig. 5) shows diffuse emission at the center, roughly aligned with the major axis of the galaxy. However, this diffuse emission is not by itself proof of the presence of a hot ISM, since an important contaminant in a galaxy like NGC821, that has a low hot gas content (Sect. 1), is the undetected portion of the LMXB population (see for example the case of NGC1316, Kim & Fabbiano 2003); another contaminant could be the emission of normal stars (first discussed for this type of galaxies in Pellegrini & Fabbiano 1994).

In this Section we report the results of the analysis of this diffuse emission. First, we analyze the merged data to estimate its spatial and spectral properties (Sections 5.1 and 5.2). Since our deep data allow for an accurate characterization of the LMXB population (Section 3), we then use these results to estimate how much of the diffuse emission could come from unresolved LMXBs below the detection threshold, comparing: (1) the shape of the radial profiles observed for the diffuse emission, the resolved point sources and the stellar optical light (Sect. 5.3); (2) the radial profile of the soft emission contributed by LMXBs and the total observed soft profile (Sect. 5.4); (3) the total luminosity of the diffuse emission with that expected from unresolved LMXBs, using the XLF derived in Sect. 3.1 (Sect. 5.5). Finally, in Sect. 5.6, we derive the expected contribution from other types of stellar sources.

5.1. Radial profile

After having excluded all the detected sources, we derived a radial profile of all the remaining counts, in the 0.3–6 keV energy band; at energies > 6 keV the background contribution becomes dominant and the addition of these photons would only increase the errorbars. The profile was centered on the nucleus, and included 30 circular annuli (each $\sim 5''$ wide). The resulting radial profile is shown in Figure 9, where the presence of emission is evident as far as $\sim 20'' - 30''$ from the nucleus ($\sim 2.3 - 3.5$ kpc at the galaxy distance of 24.1 Mpc). The flattening at larger radii is consistent with the expected background level. Therefore, diffuse emission is detected out to a radius that lies well within the optical extent of the galaxy, even within one effective radius (Tab. 1).

5.2. Spectral analysis of the diffuse emission

We analyzed the spectra of three circles centered on the galactic center, of progressively larger radius: $5''$ and $10''$, to investigate the gas presence in the circumnuclear region, and $30''$, that is the outermost radius at which

diffuse emission is detected. Prior to their extraction, we removed regions including detected sources. The background was estimated from a source-free circular area of $50''$ radius, located outside the galaxy. We fitted the spectra with single component models, such as a power law (XSPEC model *wabs * pow*) as expected from the integrated LMXB emission, and a thermal APEC model (XSPEC model *wabs*apec*), to account for the emission of a hot gas component; we then used a composite power-law and APEC model (*wabs(apec+pow)*). The results are summarized in Tab. 4; errors quoted below give the 68% confidence interval for one interesting parameter.

The spectrum of a central circle of $5''$ radius is well fitted by a single absorbed power law model, with a photon index $\Gamma = 1.77 \pm 0.17$ and N_H consistent with the Galactic value, which is in good agreement with the spectral parameters of LMXBs (Sect. 3). The thermal model also gives an acceptable fit, provided that the temperature is high ($kT \sim 5$ keV at the best fit), which again is what is expected for LMXBs (Fabbiano 2006). Next we attempted the *wabs(apec+pow)* spectral model, to probe for the presence of a hot gas component, in addition to the LMXB emission that is clearly dominant. N_H was fixed at the Galactic value and the abundance to the solar value, that is an average for the stellar population in the central galactic region (Proctor et al. 2005). At the best fit, $\Gamma = 1.61^{+0.23}_{-0.21}$ and $kT = 0.21^{+0.16}_{-0.20}$ keV; however, this fit does not represent a statistically significant improvement with respect to the simple power law model, as was established via a "calibration" of the F-test through simulations, following the prescriptions² discussed in Protassov et al. (2002; their Sect. 5.2). The analysis of the spectrum of a central circle of $10''$ radius gave similar results (Tab. 4). This spectrum is well described by a power law consistent with the average spectrum of LMXBs ($\Gamma = 1.81 \pm 0.13$ and Galactic N_H), and again a thermal component is not statistically required.

We then analyzed the spectrum of the diffuse emission from the whole galaxy (i.e., from within a radius of $30''$). Again, a simple power law model gives an acceptable fit, with $\Gamma = 1.74 \pm 0.14$. If a thermal component is added, with solar abundance and Galactic N_H , then $\Gamma = 1.59^{+0.09}_{-0.17}$ and $kT = 0.59 \pm 0.18$ keV; however, this thermal component is not required statistically. The 68% confidence upper limit on its luminosity is $L(0.3-8 \text{ keV}) < 1.34 \times 10^{38} \text{ erg s}^{-1}$. Based on the shallower pointings of 2002, David et al. (2006) estimated a 90% confidence upper limit on $L(0.5-2 \text{ keV})$ of $7.0 \times 10^{38} \text{ erg s}^{-1}$, for a thermal component.

In the analysis above the presence of a small amount of thermal emission confined to the central region might be overwhelmed by the emission of unresolved LMXBs along the line of sight. Therefore we also attempted the deprojection of the spectral data by using the technique im-

² The basic steps of the procedure consist of fitting the observed data with the simple (pow) and composite (apec+pow) models, getting the F-statistic for these fits, simulating a large number spectra for the simple best fit pow model with XSPEC, fitting each of the simulated data sets with both the simple and the composite model and recording the F-statistic, getting the distribution of the simulated F-statistic to compute a *p*-value (Protassov et al. 2002) that establishes whether the addition of the thermal spectral component is significant or not.

plemented within XSPEC, where the spectra extracted from annuli centered on the nucleus are compared with the spectra expected from the superposition along the line of sight of the emission coming from the corresponding spherical shells [as successfully done for the Sombrero bulge, Pellegrini et al. (2003b)]. The central region was therefore divided in an inner circle of $5''$ radius, a surrounding annulus with outer radius of $10''$, and another surrounding annulus of outer radius of $20''$. The spectra of each of these regions were jointly fitted with the spectral models used above. Unfortunately, the outermost annulus does not have enough counts to add meaningful spectral information, therefore only the two inner regions were deprojected. The simple power law model (*project*wabs*powerlaw*), with the photon index constrained to be the same in the two regions, gives an acceptable fit for $\Gamma = 1.68_{-0.15}^{+0.26}$ and $N_H = 2.5_{-2.5}^{+8.0} \times 10^{20} \text{ cm}^{-2}$ (inner region) and $< 4.3 \times 10^{20} \text{ cm}^{-2}$ (outer region). The addition of a thermal component [XSPEC model *project*wabs(apec+pow)*, with solar abundance and Galactic N_H] gives a best fit $\Gamma = 1.73_{-0.15}^{+0.17}$, and temperatures of $kT = 0.17_{-0.07}^{+0.06} \text{ keV}$ for the outer annulus, and $kT = 0.03_{-0.03}^{+0.09} \text{ keV}$ for the inner circle. The latter value is too small to be meaningful, therefore the fit was repeated with a fixed $\Gamma = 1.7$ (typical of LMXBs, Sect. 3). The outer temperature remained unchanged and a more meaningful temperature was obtained for the inner circle ($kT = 0.18 \text{ keV}$), but it continued to be basically unconstrained. At the best fit, the luminosity of the thermal component is $\sim 5\%$ and $\sim 13\%$ that of the power law, respectively for the inner and outer regions. However, the addition of the thermal component is not statistically significant.

In summary, the analysis of the projected regions and of the central deprojected regions never require the presence of thermal emission. A soft thermal component of luminosity much lower than that of the power law ($\sim 1/10$ at the best fit) can only be accommodated within the data uncertainties of the spectra of the $5''$, $10''$ and $30''$ circles.

5.3. Radial profiles of detected sources, diffuse emission and galactic optical emission

Figure 10 shows the comparison of the radial profiles of three quantities: (1) the background-subtracted diffuse emission in the 0.3–6 keV band, (2) the number density of resolved point sources, (3) the R-band emission of NGC821. The latter, that gives the distribution of the stellar surface brightness, is well described by a de Vaucouleurs (1948) law $I(R) \propto \exp\{-7.669 * [(R/43.9)^(1/4) - 1]\}$, where R is in arcseconds (Soria et al. 2006b).

All three profiles follow the same radial trend. The agreement between the radial profile of resolved point sources and that of the stellar light is not surprising (see, e.g., Kim & Fabbiano 2003, Fabbiano 2006). The similarity of these profiles with that of the diffuse emission provides instead support to (or at least is consistent with) the idea that also the diffuse emission mostly comes from undetected LMXBs.

5.4. Simulated (LMXB) and observed soft radial profiles

If the diffuse emission is mostly due to unresolved LMXBs, as suggested by the analysis of the previous two Sections 5.2 and 5.3, we would expect its spectrum to have a power-law shape typical of the LMXB population, at all radii. Any deviation is suggestive of a localized additional hot ISM component.

In order to further check the lack of a soft thermal component indicated by the previous analysis at all radii, we made the following test. We derived from observations the radial profile of the diffuse hard emission in the 1.5–6 keV band; in the hypothesis that it is produced by a distributed source whose spectrum is a power law of $\Gamma = 1.7$ and Galactic N_H , we then used it to derive a "simulated" radial profile in the 0.3–1.5 keV band. The chosen spectrum represents the emission of unresolved LMXBs, in accordance with the results of Sects. 3. In Figure 11 we compare the simulated soft profile with the observed profile of the diffuse emission in the same energy band. The agreement between the two profiles is good, consistent with the idea that the observed soft emission is due substantially to unresolved binaries. Only within the central circle of $10''$ radius an additional contribution from a soft source could be present, but is not revealed by the spectral analysis (Sect. 5.2).

5.5. The unresolved emission implied by the XLF

The emission from undetected LMXBs can be recovered from the XLF derived in Sect. 3.1 specifically for NGC821, as the difference between the total luminosity expected from LMXBs based on the XLF, $L_X(\text{total})$, and the luminosity due to all detected sources, $L_X(\text{detected})$. In the 0.3–8 keV band, $L_X(\text{detected}) = 6.5 \times 10^{39} \text{ erg s}^{-1}$ for the sources falling within the D25 ellipse. For the same region, $L_X(\text{total})$ is not just given by an integration of the XLF, since the XLF was derived for the D25 ellipse with a central circle of $10''$ radius excluded (Sect. 3.1). $L_X(\text{total})$ for the whole D25 ellipse is obtained rescaling the luminosity resulting³ from the XLF by the ratio between the luminosity of detected sources in the two regions (i.e., the D25 ellipse and this ellipse without the central circle). This procedure relies on the assumptions that (1) the XLF for $R < 10''$ and $R > 10''$ is the same, and (2) $L_X(\text{total})/L_X(\text{detected})$ is also the same in these two regions. While (1) is reasonable, (2) is less valid, since more sources would be hidden in the inner region. Therefore, both $L_X(\text{total})$ and $L_X(\text{undetected}) = L_X(\text{total}) - L_X(\text{detected})$ are actually lower limits. For the D25 ellipse, $L_X(\text{total})$ is $7.6 \times 10^{39} \text{ erg s}^{-1}$, and $L_X(\text{undetected}) = 1.1 \times 10^{39} \text{ erg s}^{-1}$.

It is interesting now to compare the unresolved LMXBs emission with the luminosity of the diffuse emission derived from the spectrum of a central circle of $30''$ radius (i.e., $1.4 \times 10^{39} \text{ erg s}^{-1}$, Sect. 5.2). Therefore we repeated the procedure above to calculate $L_X(\text{undetected})$ for this circle, and it turned out that $L_X(\text{undetected}) = 7.4 \times 10^{38}$

³ This integration assumes that the differential XLF has the same slope (~ 2) down to $L_X = 10^{37} \text{ erg s}^{-1}$, and is done over the range $L_X = (10^{37} - 10^{39}) \text{ erg s}^{-1}$. Given the slope value, sources of luminosities below $10^{37} \text{ erg s}^{-1}$ do not contribute significantly to the result; for example, decreasing the lower boundary by a factor of two would increase the resulting total luminosity by $\sim 15\%$. In addition, a low luminosity break in the XLF is also expected (e.g., Kim et al. 2006).

erg s⁻¹. This value is quite lower than the spectral luminosity of the diffuse emission; however, as noted above, it is likely an underestimate of the true value. Also, considering the uncertainty in the normalization of the XLF ($k = 8.4_{-2.5}^{+3.1}$, Sect. 3.1), L_X (undetected) can be as large as 2.7×10^{39} erg s⁻¹.

In summary, for the same circle of $R = 30''$, the spectral luminosity of the diffuse emission and the XLF-based unresolved luminosity are close, and they agree within the uncertainties.

5.6. Other stellar sources

Since we are constraining the origin of the diffuse emission in NGC821 better than it has been possible so far in previous analyses of low L_X/L_B ellipticals, we check also for the amount of diffuse emission that can be accounted for by stellar sources other than LMXBs. In the old stellar population of an elliptical galaxy these include coronae of late type main sequence stars, RS Canum Venaticorum (RS CVn) systems and supersoft X-ray sources (Pellegrini & Fabbiano 1994). The latter are characterized by black body emission with effective temperatures of 15–80 eV, X-ray luminosities up to few $\times 10^{38}$ erg s⁻¹ and are more frequent in late type and irregular galaxies (Kahabka & van den Heuvel 1997; Di Stefano & Kong 2004). NGC4697 is the only elliptical where they have been identified so far (Sarazin et al. 2001). In the X-ray color-color plot of NGC821 (Fig. 2), supersoft sources would fall in the upper right corner, and there is no such source with > 30 counts; one or two sources with less than 30 counts have a high C32 color, but with a large error. The contribution of supersoft sources will not be considered further here.

Stellar coronae of main sequence stars are all sources of thermal X-ray emission ($L_X \approx 10^{26} - 10^{30}$ erg s⁻¹) indicative of coronal plasmas at temperatures of $\sim 10^6 - 10^7$ K (e.g., Schmitt et al. 1990). These luminosities are faint in comparison to accretion powered stellar sources, but main sequence stars of spectral types G, K and M are present in a very large number (hereafter respectively N_G , N_K and N_M). These N_i can be recovered from the initial stellar mass function (IMF) $\psi(M) = AM^{-2.35}$ (Salpeter 1955), where the scale-factor $A = 1.66L_B$, with L_B in $L_{B,\odot}$, for a 12 Gyrs old stellar population with a 0.5 solar metallicity (Maraston 2005), as suitable for NGC821 (Proctor et al. 2005). Note that A does not vary more than (10 – 15)% for old and metal-rich stellar populations typical of elliptical galaxies. Then $N_i = A \int_{M_{inf}}^{M_{sup}} M^{-2.35} dM$, where M_{inf} and M_{sup} are respectively $0.7M_\odot$ and the main sequence turn-off mass of $0.9M_\odot$ (as appropriate for NGC821, according to the stellar evolutionary tracks of Girardi et al. 2000) for G stars; 0.5 and $0.7M_\odot$ for K stars; and 0.08 and $0.5M_\odot$ for M stars. Integration gives $N_G = 0.55L_B$, $N_K = 1.10L_B$ and $N_M = 32.8L_B$, therefore the collective M dwarf X-ray emission is by far the most important, because the average X-ray luminosity of a G, K and M star (hereafter $L_{X,M}$) are comparable (Kuntz & Snowden 2001). Taking $L_{X,M} \lesssim 1.4 \times 10^{27}$ erg s⁻¹ in the 0.3–8 keV band⁴, the collective M dwarfs emis-

sion in NGC821 is then $N_M \times L_{X,M} \lesssim 8.6 \times 10^{38}$ erg s⁻¹. From a central circle of $30''$ radius, for the de Vaucouleurs optical profile of Sect. 5.3, the M dwarfs emission is $\lesssim 3.4 \times 10^{38}$ erg s⁻¹, that is $\lesssim 24\%$ of the luminosity derived from the spectrum of the diffuse emission from the same region (Sect. 5.2). However, recent claims favor an IMF flatter than the Salpeter one at the low mass end, as for the Kroupa (2001) IMF, which is $\propto M^{-1.8}$ for $0.08 \leq M/M_\odot \leq 0.5$. In this case the scale-factor A is practically unchanged (Maraston 2005), the integration gives $N_M = 12.3L_B$, and the collective M dwarfs emission becomes $\lesssim 3.2 \times 10^{38}$ erg s⁻¹ for the whole galaxy, and $\lesssim 1.3 \times 10^{38}$ erg s⁻¹ for a circle of $30''$ radius. Therefore, it can account for $\lesssim 9\%$ of the luminosity of the diffuse emission.

RS CVn systems are chromospherically active objects, consisting of a G or K giant or subgiant, with a late type main sequence or subgiant companion (Linsky 1984). They are the most X-ray luminous late type stars ($L_X \sim 10^{29} - 10^{31.5}$ erg s⁻¹), and their spectra can be well modeled by a thermal plasma with two temperatures (of average $kT = 1.3$ keV and 0.18 keV, Dempsey et al. 1997). From Dempsey et al.'s Fig. 3, the average 0.3–8 keV luminosity of a system is⁵ $\lesssim 3 \times 10^{30}$ erg s⁻¹. The number of RS CVn systems is a fraction of the number of giants and subgiants (respectively N_{giant} and N_{subg}) expected to be present in NGC821, which is⁶ $N_{subg} + N_{giant} \approx 0.04L_B$. Taking half this number for those giants or subgiants that are also in binary systems, and another factor (~ 0.2) for those that become RS CVn, then the collective contribution is $\lesssim 0.1(N_{subg} + N_{giant}) \times 3 \times 10^{30}$ erg s⁻¹ = $1.2 \times 10^{28} L_B$ erg s⁻¹. This is $\lesssim 2.2 \times 10^{38}$ erg s⁻¹ for the whole galaxy, and $\lesssim 8.9 \times 10^{37}$ erg s⁻¹ from a circle of $30''$ radius, that is $\lesssim 6\%$ of the total diffuse emission within the same region.

In conclusion, the collective emission of stellar sources other than LMXBs from the whole galaxy is $\lesssim 5.4 \times 10^{38}$ erg s⁻¹; as expected, this is much smaller than the collective LMXB's emission (7.6×10^{39} erg s⁻¹, Sect. 5.5), but even smaller than its unresolved fraction [i.e., L_X (undetected) = 1.1×10^{39} erg s⁻¹, Sect. 5.5]. Also, these sources account for $\lesssim 15\%$ of the diffuse emission detected within a radius of $30''$. Their average spectrum is quite softer than that of LMXBs, therefore their contribution to the diffuse emission, if any, will lower further the limit on the hot gas presence [for which $L(0.3-8 \text{ keV}) < 1.34 \times 10^{38}$ erg s⁻¹, Sect. 5.2].

5.7. Conclusions on hot gas presence

keV when converting $L_{X,M}$ in the *ROSAT* band (Kuntz & Snowden 2001) to the 0.3–8 keV band. The proper spectral description consists of two thermal components: one with $T \sim 2 - 4 \times 10^6$ K and the other with $T \sim 10^7$ K; the latter usually has larger (and often much larger) emission measure (Giampapa et al. 1996).

⁵ Again the \lesssim sign comes from assuming that most of the emission is due to the higher temperature component.

⁶ N_{giant} and N_{subg} are the product of the time spent by stars in such evolutionary phases by the specific evolutionary flux for a 12 Gyr old stellar population (which is fairly independent of the IMF; Maraston 2005) and by L_B . Low mass metal rich stars spend 7×10^8 yrs in the G/K-subgiant phase, and 5×10^8 Gyr on the red giant branch (e.g., Renzini 1989).

⁴ The \lesssim sign comes from assuming thermal emission of $kT = 1$

All the different lines of investigation undertaken in this Section consistently indicate a largely dominating LMXB contribution to the diffuse X-ray emission. Its spectrum does not require soft thermal emission, that is limited to $< 1.34 \times 10^{38} \text{ erg s}^{-1}$ ($< 10\%$ of the total diffuse luminosity) at 68% confidence. The observed radial profiles of the stellar light, the resolved point sources and the diffuse emission agree within the errors, suggesting that the diffuse emission has a stellar origin. The observed radial profile in the soft band is consistent with that expected from the sources (the LMXB population) producing the hard emission, except perhaps for the innermost ($R \lesssim 10''$) region. Finally, the luminosity of undetected sources derived from the bias-corrected XLF agrees with the spectral luminosity of the diffuse emission, within the uncertainties. A fraction of the diffuse emission ($\lesssim 15\%$) can also come from stellar sources other than LMXBs; their soft nature limits further the possibility of hot gas presence.

6. DISCUSSION

In the previous Sections we have reported the results of the analysis of a deep *Chandra* pointing (for a total exposure of nearly 230 ks) aimed at detecting the nuclear emission and setting stringent constraints on the presence of hot gas both on the circumnuclear and the galactic scale. The deep *Chandra* image revealed a significant portion of the LMXB population, for which the X-ray Luminosity Function was derived. This, together with a spectral and imaging analysis of the diffuse emission, severely constrained the presence of a hot ISM (Sect. 5). At the galactic center, in addition to diffuse emission (which we can explain as predominantly due to unresolved LMXBs), we find four sources of $L_X = (2 - 9) \times 10^{38} \text{ erg s}^{-1}$. We have been able to establish that one of these sources (S2) is coincident with the galactic center. Three of these source, including S2, are extended, with one of them as long as $5''$ (S1; Fig. 6). These sources could be truly extended, or made of one or more point-like components, possibly also embedded in truly diffuse emission. Their spectral shape is consistent with that of LMXBs, but in NGC821 there are only 3 other sources as bright as these, outside the central circle of $10''$ radius (Fig. 3). This supports the idea that more than one LMXB is contributing to the emission of each source. An alternative possibility is that they belong to a continuous complex feature, made of LMXBs (that may also lie there due to a projection effect), a nucleus (possibly with associated extended emission) and an outflow/jet. S1, in particular, has a linear structure suggestive of a jet (Fig. 6). Our VLA observations (Sect. 1) help better address these possibilities, and are presented in the companion paper (Pellegrini et al. 2006), together with a discussion on whether/how accretion proceeds in this nucleus, based on all the available observational evidence. We estimated here a 3σ upper limit to the 0.3–8 keV emission of a point-like source associated with the MBH of $< 2.8 \times 10^{38} \text{ erg s}^{-1}$, which makes this one of the quietest MBH studied with *Chandra* (e.g., Pellegrini 2005b), with $L_X/L_{Edd} < 2.5 \times 10^{-8}$.

In the following we discuss the possibility that there may be undetected hot gas in NGC 821 (Sect. 6.1). Hidden hot gas on the nuclear scale could be a source of fuel for the MBH; furthermore, we check whether the lack of

detection on the galactic scale agrees with expectations for the evolution of the ISM in this elliptical.

6.1. Is there hot undetected gas?

The present analysis does not detect hot gas available for accretion at the nucleus; coupled with the absence of interstellar medium observed at other wavelengths (Sect. 1), the lack of fuel for the MBH could be the simplest explanation for the very low levels to which the nuclear emission has been constrained. However, an aging stellar population continuously returns gas to the ISM, via stellar mass losses (e.g., Ciotti et al. 1991, David et al. 1991); as a minimum, the circumnuclear region should be replenished with this fuel. Below we consider the possible presence of this ISM.

The lack of detection of hot gas on the galactic scale can be expected from simple energetic considerations, comparing the energy made available per unit time by type Ia supernova explosions (L_{SN}) with the energy required to steadily extract from the galactic potential well the stellar mass losses produced per unit time (L_{grav} ; Ciotti et al. 1991), for the whole galaxy lifetime. L_{SN} comes directly from the observed SNIa's explosion rate in ellipticals (Cappellaro et al. 1999) rescaled for L_B in Tab. 1; this rate was higher in the past (e.g., Greggio 2005). L_{grav} derives from the stellar mass loss rate and the galactic mass profile, that can be well modelled by the superposition of two Hernquist (1990) density profiles⁷, one for the stars with total mass M_* , and one for the dark matter with mass M_h . This model is then tailored onto NGC821 taking the observed L_B , R_e , central stellar velocity dispersion (Tab. 1) and M_h/M_* ratio. Anisotropic Jeans models reproducing the observed velocity dispersion profiles of stars and planetary nebulae out to $5R_e$ constrain the range of $(M_h + M_*)/L_B$ to be 13–17 (Romanowsky et al. 2003). For a plausible stellar mass-to-light ratio M_*/L_B (Gerhard et al. 2001, Napolitano et al. 2005) one derives $M_h/M_* \sim 1.2$. Finally, the stellar mass loss rate, which is distributed as the stars, can be calculated by summing the mass ejected by each star as a function of its mass (Renzini & Ciotti 1993) for a Kroupa IMF, scaled for NGC821 as described in Sect. 5.6; this produces a total mass loss rate of $0.25 M_\odot \text{ yr}^{-1}$ after 12 Gyrs, in good agreement with the values estimated for ellipticals from *ISO* observations (Athey et al. 2002). The resulting $L_{SN} \sim (3 - 4)L_{grav}$ during the galaxy lifetime, with $L_{SN} \sim 4L_{grav}$ at present; therefore type-Ia SNe have always provided the heating to drive the stellar mass losses in a galactic wind (neglecting the effect of radiative cooling that is not expected to be important for very low gas densities typical of a wind).

However, this is a global energetic calculation, and the galaxy may host regions with $L_{SN} > L_{grav}$ and regions with $L_{SN} < L_{grav}$. For centrally peaked mass distributions like those described above, numerical simulations of hot gas evolution showed that this is indeed the most fre-

⁷ This model gives a very good approximation of the de Vaucouleurs (1948) law, that fits the light profile of NGC821 (Sect. 5.3). The radial distribution of the dark haloes of ellipticals is not well constrained by the observations. Theoretical arguments favor a peaked profile (Ciotti & Pellegrini 1992; Evans & Collett 1997). High resolution numerical simulations (Navarro, Frenk, & White 1996) produce a central density distribution equal to that of the Hernquist model.

quent case (Pellegrini & Ciotti 1998): the ISM is driven out of the outer galactic regions in a wind, while it is inflowing within a stagnation radius that can be largely different from galaxy to galaxy. To explore whether this situation applies to NGC 821, we ran hydrodynamical simulations specific for the galaxy model described above, plus the additional gravitational attraction contributed by its central MBH (see Pellegrini & Ciotti 2006 for more details on the numerical code and the time-evolving input quantities). The central grid spacing was set to 5 pc to allow for a better sampling of the inner regions and the gas flow evolution was followed for 12 Gyrs, an age comparable with the stellar age of NGC 821 (Proctor et al. 2005). The flow kept in a partial wind all the time, with the bulk of the hot gas outflowing, so that at the end its total $L_X \sim \text{few} \times 10^{36} \text{ erg s}^{-1}$ in the 0.3–8 keV band, well below our observational limit on the hot gas. The gas flow is directed towards the center from within a radius of ~ 25 pc. At the smallest radius at which the flow is well resolved (10 pc) the mass inflow rate is $\dot{M}_{in} \approx \text{few} \times 10^{-5} M_\odot \text{ yr}^{-1}$, and the gas density is $n_e \approx 10^{-3} \text{ cm}^{-3}$; this is one third of the value calculated from the emission measure of the "best fit" thermal component for the central circle, in the deprojected analysis of the diffuse emission (Sect. 5.2). Note however that the inflowing region is very small and fully included within the extent of the S2 source (Sect. 4.1). By varying the M_h/M_* ratio, the SNIa's rate, the age of the galaxy and the stellar mass loss rate within the limits imposed by observational uncertainties, the value of \dot{M}_{in} keeps within the range $(2 - 7) \times 10^{-5} M_\odot \text{ yr}^{-1}$. The implications for the nuclear emission coming from this estimate of \dot{M}_{in} are discussed in Pellegrini et al. (2006). Here we just note that \dot{M}_{in} ranges from 10^{-3} to $\text{few} \times 10^{-5} M_\odot \text{ yr}^{-1}$ in the past ~ 10 Gyrs. By integration of its values over this time, the total mass accreted at the center is $\sim 2 \times 10^6 M_\odot$, that is 2.3×10^{-2} of the observed MBH mass (Tab. 1). Therefore, accretion of stellar mass losses was not effective in building this MBH mass.

Finally, we comment on the fact that, by using *Chandra* observations, the mass accretion rate of galactic nuclei is customarily estimated from the analytic formula of Bondi (1952), valid for spherically symmetric accretion from a nonrotating polytropic gas with given density and temperature at infinity (e.g., Loewenstein et al. 2001, Soria et al. 2006a). Infinity is replaced with an accretion radius $r_{acc} = 2GM_{BH}/c_s^2$ (Frank et al. 2002), where the sound speed $c_s \propto \sqrt{kT}$ is calculated as close as possible to the MBH. Even in those cases where kT can be observed close to the galactic center, so that one can be confident to derive an approximate estimate of r_{acc} , there are additional ingredients that must be considered in the estimate of the mass accretion rate, which were not included in the Bondi (1952) treatment: 1) the presence of mass and energy sources (i.e., stellar mass losses and SNIa's heating); 2) the presence of cooling; 3) the fact that r_{acc} is not a true "infinity" point, since the gas here experiences a pressure gradient. The simulations described here take into account all these aspects, and should give a more reliable mass accretion rate than the Bondi theory. However, they have some limits too. At these very low \dot{M}_{in} values, and very small inflowing

regions, the true shape of the galactic mass profile becomes important. In the case of NGC821, the observed profile is steeper than modelled here at the very center (Gebhardt et al. 2003), which should produce a larger \dot{M}_{in} . The true accretion rate could be somewhat higher than \dot{M}_{in} also if even the stellar mass losses within the innermost radius resolved by the simulations are to be accreted. But further pursuing the flow behavior closer to the MBH runs into a problem: the discrete nature of the stellar distribution becomes important, since the accretion time ($\sim 3 \times 10^5$ yrs from 10 pc, in the simulations) becomes comparable to (or lower than) the time required for the stellar mass losses to mix with the bulk flow (Mathews 1990), and the time elapsing between one SNIa event and the next.

7. SUMMARY

We have observed the nearby, inactive elliptical galaxy NGC821, known to host a central MBH, with deep *Chandra* pointings, in order to put strong constraints on its nuclear emission and the presence of gas available for accretion. Our results can be summarized as follows:

1. We detect 41 sources within the optical size of the galaxy, representing the LMXB population of NGC 821. The X-ray colors of these sources are consistent with spectral shapes described by power laws of photon index in the range $\Gamma = 1.5 - 2.0$, without intrinsic absorption. There is no clear evidence for supersoft sources.
2. The XLF of these sources is well fitted by a simple power law down to $L_X = 3 \times 10^{37} \text{ erg s}^{-1}$, with a slope ($\beta = 2.0 \pm 0.3$) similar to that found previously for other ellipticals. The ratio between the total L_X due to LMXBs and the galactic L_B is lower than the average found for early-type galaxies, but still within the observed scatter.
3. At the position of the galactic center a source (S2) is detected for the first time. Its spectral shape is quite hard ($\Gamma = 1.49^{+0.14}_{-0.13}$), without intrinsic absorption. S2 is however extended, and a 0.3–8 keV upper limit of $2.8 \times 10^{38} \text{ erg s}^{-1}$ is derived for a point-like nuclear source, one of the smallest established with *Chandra*.
4. Three other sources, with a spectral shape typical of LMXBs, are detected in the central galactic region; they are as bright as the brightest sources in the XLF. Only one (S3) is consistent with being pointlike; the other two (S1 and S4) are extended, and could be due to the superposition of few LMXBs and/or truly diffuse emission. The morphology of S1 resembles a jet-like feature.
5. Diffuse emission is detected out to a radius of $\sim 30''$. A few independent lines of investigation, exploiting the spectral and imaging capabilities of *Chandra*, consistently indicate that this diffuse emission is due to unresolved LMXBs, and provide no evidence for hot gas, either close to the center or on a larger scale. The spectral analysis gives a (1σ) limit of $L(0.3-8 \text{ keV}) < 1.34 \times 10^{38} \text{ erg s}^{-1}$ on any soft thermal component within a radius of $30''$.

6. Other unresolved stellar sources (mostly M dwarfs and RS CVn systems) could contribute to the diffuse emission by $\lesssim 15\%$. The general scaling of their collective L_X with the galactic L_B for ellipticals was also derived.
7. Numerical simulations of the hot gas evolution for a galaxy model tailored on NGC 821 show that the bulk of the gas is driven out in a wind for the whole galaxy lifetime, due to the heating provided by type Ia supernovae. While this may have been expected based on simple energetic calculations, the simulations also show that the gas is accreting towards the center from within a very small inner region. This gas flow pattern is expected to be common in low L_B ellipticals, due to their cuspy central mass distribution. Gaseous accretion alone at the rates given by the simulations cannot have formed the nuclear MBH of NGC821.

In a companion paper (Pellegrini et al. 2006), we present further observational results for the central region of NGC 821, obtained with *Spitzer* and the VLA, and discuss various possibilities for the nature of the accretion process in this very low luminosity nucleus.

We thank F. Ferraro for useful information related to Sect. 5.6. S.P. acknowledges partial financial support from the Italian Space Agency ASI (Agenzia Spaziale Italiana) through grant ASI-INAF I/023/05/0. Partial support for this work was provided by the NASA *Chandra* Guest Observer grant GO5-6110X and by the *Chandra* X-ray Center NASA contract NAS8-39073. The data analysis was supported by the CXC CIAO software and CALDB. We have used NASA NED and ADS facilities, and have extracted archival data from the Hubble Space Telescope archive.

REFERENCES

- Anders, E., Grevesse, N. 1989, *Geochim. Cosmochim. Acta* 53, 197
- Athey, A., Bregman, J., Bregman, J., Temi, P., Sauvage, M. 2002, *ApJ* 571, 272
- Bender, R., Saglia, R. P., Gerhard, O. E. 1994, *MNRAS* 269, 785
- Bondi, H. 1952, *MNRAS*, 112, 195
- Cappellaro, E., Evans, R., Turatto, M. 1999, *A&A* 351, 459
- Ciotti L., D'Ercole A., Pellegrini S., Renzini A. 1991, *ApJ* 376, 380
- Ciotti, L., Pellegrini, S. 1992, *MNRAS* 255, 561
- Ciotti, L., & Ostriker, J.P. 2001, *ApJ*, 551, 131
- Cutri, R. M., Skrutskie, M. F., van Dyk, S., et al. 2003, The IRSA 2MASS All-Sky Point Source Catalog, NASA/IPAC Infrared Science Archive.
<http://irsa.ipac.caltech.edu/applications/Gator/>
- David, L.P., Forman, W., Jones, C. 1991, *ApJ* 369, 121
- David, L.P., Jones, C., Forman, W., Vargas, I.M., Nulsen, P. 2006, *ApJ* 653, 207
- Dempsey, R.C., Linsky, J.L., Fleming, T.A., Schmitt, J.H.M.M., 1997, *ApJ*, 478, 358
- de Vaucouleurs G., 1948, *Ann.Ap.*, 11, 247
- de Vaucouleurs G., de Vaucouleurs A., Corwin Jr. H.G., Buta R.J., Paturel G., Fouque P., 1991, *Third Reference Catalogue of Bright Galaxies*, (New York: Springer Verlag) (RC3)
- Dickey, J. M., Lockman, F. J. 1990, *ARA&A* 28, 215
- Di Matteo, T., Allen, S.W., Fabian, A.C., Wilson, A.S., & Young, A. J. 2003, *ApJ*, 582, 133
- Di Stefano, R., Kong, A. 2004, *ApJ* 609, 710
- Eddington, A.S. 1913, *MNRAS* 73, 359
- Evans, N. W., Collett, J. L. 1997, *ApJ* 480, L103
- Fabbiano, G., Elvis, M., Markoff, S., Siemiginowska, A., Pellegrini, S., Zezas, A., Nicastro, F., Trinchieri, G., & McDowell, J. 2003, *ApJ* 588, 175
- Fabbiano, G., Baldi, A., Pellegrini, S., Siemiginowska, A., Elvis, M., Zezas, A., & McDowell, J. 2004, *ApJ*, 616, 730 (F04)
- Fabbiano, G. 2006, *ARA&A* 44, 323
- Fabian, A.C., & Canizares, C.R. 1988, *Nature*, 333, 829
- Ferrarese, L., Ford, H. 2005, *Space Science Reviews* 116, 523
- Frank, J., King, A., & Raine, D. 2002, *Accretion Power in Astrophysics*, Cambridge: CUP
- Gebhardt, K., Richstone, D., Tremaine, S., et al. 2003, *ApJ*, 583, 92
- Gerhard O., Kronawitter, A., Saglia, R. P., Bender, R. 2001, *AJ* 121, 1936
- Giampapa, M. S., Rosner, R., Kashyap, V., Fleming, T. A., Schmitt, J. H. M. M., Bookbinder, J. A. 1996, *ApJ* 463, 707
- Gilfanov, M. 2004, *MNRAS* 349, 146
- Girardi, L., et al., 2000, *A&AS* 141, 371
- Greggio, L., 2005, *A&A* 441, 1055
- Hernquist L.E., 1990, *ApJ*, 536, 359
- Ho, L.C. 2005, *Ap&SS* 300, 219
- Irwin, J., Athey, A., Bregman, J. 2003, *ApJ* 587, 356
- Kahabka, P., van den Heuvel, E. 1997, *ARA&A* 35, 69
- Kim D.W., Fabbiano G., Trinchieri G. 1992, *ApJ* 393, 134
- Kim, D.W., & Fabbiano, G. 2003, *ApJ*, 586, 826
- Kim, D.W., & Fabbiano, G. 2004, *ApJ*, 611, 846
- Kim, D.W., Wilkes, B., Green, P., et al. 2004, *ApJ*, 600, 59
- Kim, D.W., Fabbiano, G., Kalogera, V., et al. 2006, *ApJ* 652, 1090
- Kim, M., Wilkes, B.J., Kim, D.W., Green, P.J., Barkhouse, W.A., Lee, M.G., Silverman, J.D., Tananbaum, H.D. 2006, *ApJ* in press (astro-ph/0611841)
- Kroupa, P. 2001, *MNRAS* 322, 231
- Kuntz, K.D., Snowden, S.L. 2001, *ApJ* 554, 684
- Lauer T.R., et al. 2005, *AJ* 129, 2138
- Linsky, J.L., 1984. In *Cool Stars, Stellar Systems and the Sun*, eds. S.L. Baliunas and L. Hartmann (Berlin: Springer Verlag), p.244
- Loewenstein, M., Mushotzky, R.F., Angelini, L., Arnaud, K.A., & Quataert, E. 2001, *ApJ*, 555, L21
- Maraston, C. 2005, *MNRAS* 362, 799
- Mathews, W. 1990, *ApJ* 354, 468
- Monet, D. G., Levine, S.E., Canzian, B., et al. 2003, *AJ* 125, 984
- Napolitano, N. R., Capaccioli, M., Romanowsky, A. J., et al. 2005, *MNRAS* 357, 691
- Navarro, J.F., Frenk, C.S., White, S.D. M. 1996, *ApJ* 462, 563
- Omma, H., Binney, J., Bryan, G., & Slyz, A. 2004, *MNRAS*, 348, 1105
- O'Sullivan, E., Forbes, D.A., Ponman, T.J. 2001, *MNRAS* 328, 461
- Pellegrini S., Fabbiano, G. 1994, *ApJ* 429, 105
- Pellegrini S., Ciotti L. 1998, *A&A* 333, 433
- Pellegrini S., Venturi, T., Comastri, A., Fabbiano, G., Fiore, F., Vignali, C., Morganti, R., Trinchieri, G. 2003a, *ApJ* 585, 677
- Pellegrini S., Baldi, A., Fabbiano, G., Kim, D.W. 2003b, *ApJ* 597, 175
- Pellegrini, S. 2005a, *ApJ*, 624, 155
- Pellegrini, S. 2005b, *MNRAS* 364, 169
- Pellegrini, S., Ciotti, L. 2006, *MNRAS* 370, 1797
- Pellegrini, S., Siemiginowska, A., Fabbiano, G., Greenhill, L., Soria, R., Elvis, M., Baldi, A., Kim, D.W. 2006, submitted to *ApJ*
- Pinkney, J., Gebhardt, K., Bender, R., et al. 2003, *ApJ* 596, 903
- Proctor, R. N., Forbes, D. A., Forestell, A., Gebhardt, K. 2005, *MNRAS* 362, 857
- Protassov, R., van Dyk, d.A., Connors, A., Kashyap, V.L., Siemiginowska, A. 2002, *ApJ* 571, 545
- Rees, M. 1984, *ARA&A* 22, 471
- Renzini, A., 1989. In *Evolutionary Phenomena in Galaxies*, ed. J. Beckman, and B. Pagel (Cambridge University Press), p. 422
- Renzini, A., Ciotti, L. 1993, *ApJ* 416, L49

- Romanowsky, A. J., Douglas, N. G., Arnaboldi, M., et al. 2003, *Science* 301, 1696
- Salpeter, E.E. 1955, *ApJ* 121, 161
- Sansom A.E., O'Sullivan E., Forbes D., Proctor R.N., Davis D. 2006, in press on *MNRAS* (astro-ph/0605506)
- Sarazin, C., Irwin, J., Bregman, J. 2001, *ApJ* 556, 533
- Sarzi, M., Falcon-Barroso, J., Davies, R.L., et al. 2006, *MNRAS* 366, 1151
- Schmitt, J., Collura, A., Sciortino, S., Vaiana, G., Harnden, F.R., Rosner, R. 1990, *ApJ* 365, 704
- Siemiginowska, A., Smith, R. K., Aldcroft, T. L., Schwartz, D. A., Paerels, F., Petric, A.O. 2003, *ApJ* 598, L15
- Skrutskie, M.F., Cutri, R.M., Stiening, R. et al. 2006, *AJ* 131, 1163
- Smith, R.M., Martinez, V.J., Graham, M. J. 2004, *ApJ* 617, 1017
- Soria, R., Fabbiano, G., Graham, A., Baldi, A., Elvis, M., Jerjen, H., Pellegrini, S., Siemiginowska, A. 2006a, *ApJ* 640, 126
- Soria, R., Graham, A., Fabbiano, G., Baldi, A., Elvis, M., Jerjen, H., Pellegrini, S., Siemiginowska, A. 2006b, *ApJ* 640, 143
- Springel, V., Di Matteo, T., Hernquist, L. 2005, *ApJ* 620, L79
- Tonry, J.L., Dressler, A., Blakeslee, J.P., et al. 2001, *ApJ*, 546, 681
- Vikhlinin, A., Schulz, N., Tibbetts, K., Edgar, R. 2003, Corrections for Time Dependence of ACIS Gain, <http://cxc.harvard.edu/contrib/alexey/tgain/tgain.html>
- Weisskopf, M., Tananbaum, H., Van Speybroeck, L., & O'Dell, S. 2000, *Proc. SPIE*, 4012, 2

TABLE 1
NGC 821: MAIN PROPERTIES

Type ^a	B_T^0 ^a (mag)	D ^b (Mpc)	$\log L_B$ ($L_{B,\odot}$)	Size ^a (arcmin)	R_e ^c (",kpc)	σ_e ^d (km s ⁻¹)	N_H ^e (cm ⁻²)	M_{BH} ^f ($10^7 M_\odot$)	1'' (pc)
E6	11.72	24.1	10.27	2.57x1.62	43.9, 5.1	209	6.2×10^{20}	8.5 ± 3.5	117

^a Type, B_T^0 and size from de Vaucouleurs et al. (1991; RC3). The size gives the major and minor axis of the D25 ellipse, that is the 25.0 B-mag/square arcsec isophote. The position angle is 25° (RC3).

^b Distance D from Tonry et al. (2001).

^c Effective radius R_e in the R-band (from Soria et al. 2006b; see also Sect. 5.3).

^d Effective stellar velocity dispersion (averaged over R_e) from Pinkney et al. (2003).

^e Galactic hydrogen column density (Dickey & Lockman 1990).

^f Gebhardt et al. (2003) report a value of $3.7_{-0.8}^{+2.4} \times 10^7 M_\odot$, later revised to the value given here (Richstone et al., astro-ph/0403257) that is considered more reliable (Gebhardt, K. 2006, private communication).

TABLE 2
Chandra ACIS-S OBSERVING LOG FOR NGC 821.

Obs ID	Date	Exposure (ks)
4408	2002, Nov 26	25.3
4006	2002, Dec 01	13.7
5692	2004, Dec 04	28.0
6314	2005, Jun 20	40.1
6310	2005, Jun 21	32.4
6313	2005, Jun 22	50.1
5691	2005, Jun 23	40.1

TABLE 3
SPECTRAL ANALYSIS RESULTS FOR THE NUCLEAR SOURCES S1–S4.

	S1	S2	S3	S4
Net counts	178±14	246±16	324±18	82±9
<i>wabs(pow)</i> :				
N_H (10^{21} cm $^{-2}$)	$1.7^{+0.8}_{-1.0}$	< 0.5	$2.6^{+0.5}_{-0.6}$	$3.0^{+1.3}_{-1.5}$
Γ	$1.80^{+0.35}_{-0.23}$	$1.49^{+0.14}_{-0.13}$	$2.23^{+0.23}_{-0.17}$	$2.28^{+0.52}_{-0.34}$
χ^2/dof	7.3/6	11.5/9	15.8/12	2.1/5
Flux (10^{-15} erg cm $^{-2}$ s $^{-1}$)	5.8	8.6	9.1	2.3
Luminosity (10^{38} erg s $^{-1}$)	4.7	6.0	9.0	1.9
<i>wabs(apec)</i> :				
N_H (10^{21} cm $^{-2}$)	< 1.1	< 0.5	$0.9^{+0.6}_{-0.5}$	$1.4^{+1.5}_{-1.3}$
kT (keV)	$5.3^{+4.7}_{-1.8}$	$8.5^{+11}_{-3.4}$	$4.3^{+1.0}_{-0.8}$	$3.4^{+2.2}_{-0.9}$
χ^2/dof	7.0/6	11.9/9	18.4/12	1.9/5
Flux (10^{-15} erg cm $^{-2}$ s $^{-1}$)	5.7	8.1	9.7	2.4
Luminosity (10^{38} erg s $^{-1}$)	4.3	5.6	7.6	1.7

NOTE. — The N_H values are in addition to the Galactic one. Fluxes are observed values, luminosities are corrected for absorption, and are calculated for the 0.3–8 keV band. Errors give the 68% confidence interval for one interesting parameter.

TABLE 4
SPECTRAL ANALYSIS OF THE DIFFUSE EMISSION (PROJECTED REGIONS).

Radius	Net counts	Γ	F(0.3–8 keV) (10^{-15} erg cm $^{-2}$ s $^{-1}$)	L(0.3–8 keV) (10^{38} erg s $^{-1}$)	kT (keV)	F(0.3–8 keV) (10^{-15} erg cm $^{-2}$ s $^{-1}$)	L(0.3–8 keV) (10^{38} erg s $^{-1}$)	χ^2/dof
5''	166 \pm 13	1.77 $^{+0.17}_{-0.17}$	8.4 \pm 0.8	6.7 \pm 0.7	–	–	–	8.6/9
		1.61 $^{+0.23}_{-0.21}$	8.6 \pm 1.2	6.7 \pm 1.0	0.21 $^{+0.16}_{-0.20}$	0.37 $^{+13.6}_{-0.18}$	0.44 $^{+16.2}_{-0.22}$	7.4/7
10''	175 \pm 16	1.81 $^{+0.13}_{-0.13}$	9.8 \pm 0.7	7.9 \pm 0.6	–	–	–	25.0/19
		1.57 $^{+0.12}_{-0.15}$	10.0 \pm 1.4	7.8 \pm 1.1	0.25 $^{+0.08}_{-0.06}$	0.69 $^{+0.35}_{-0.32}$	0.75 $^{+0.38}_{-0.35}$	21.9/17
30''	581 \pm 48	1.74 $^{+0.14}_{-0.14}$	17.9 \pm 1.3	14.3 \pm 1.10	–	–	–	78.2/64
		1.59 $^{+0.09}_{-0.17}$	16.9 $^{+3.1}_{-2.3}$	13.0 $^{+2.40}_{-1.70}$	0.59 $^{+0.18}_{-0.18}$	1.06 $^{+0.42}_{-0.71}$	0.96 $^{+0.38}_{-0.64}$	71.9/62

N_H is fixed at the Galactic value of 6.2×10^{20} cm $^{-2}$ (Tab. 1); in the *apec* spectral model, the abundance is fixed at the solar value. Fluxes are observed, luminosities are intrinsic. Errors give the 68% confidence range for one interesting parameter.

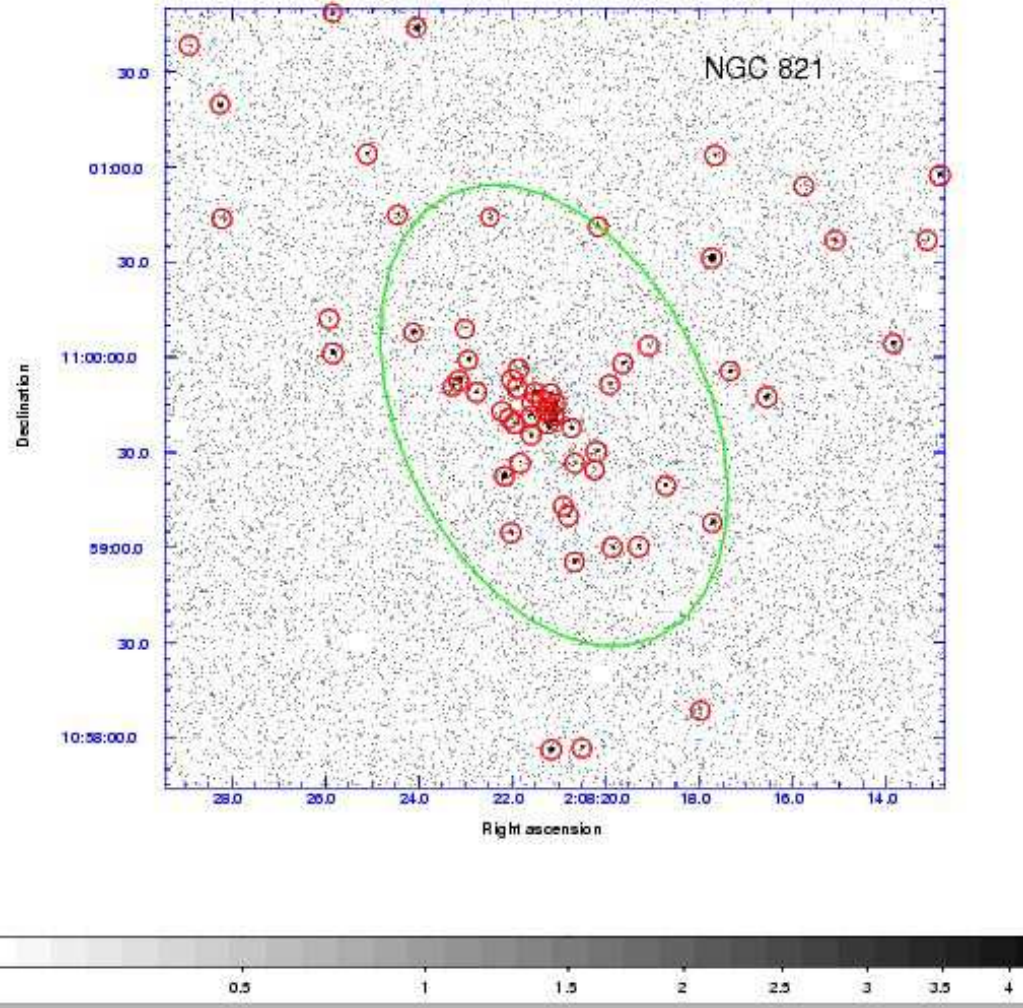


FIG. 1.— Merged ACIS-S image of NGC821, with the D25 ellipse of Table 1 overplotted in green and the X-ray sources detected by *wavdetect* marked in red with circles of $3''$ radii (Sect. 3).

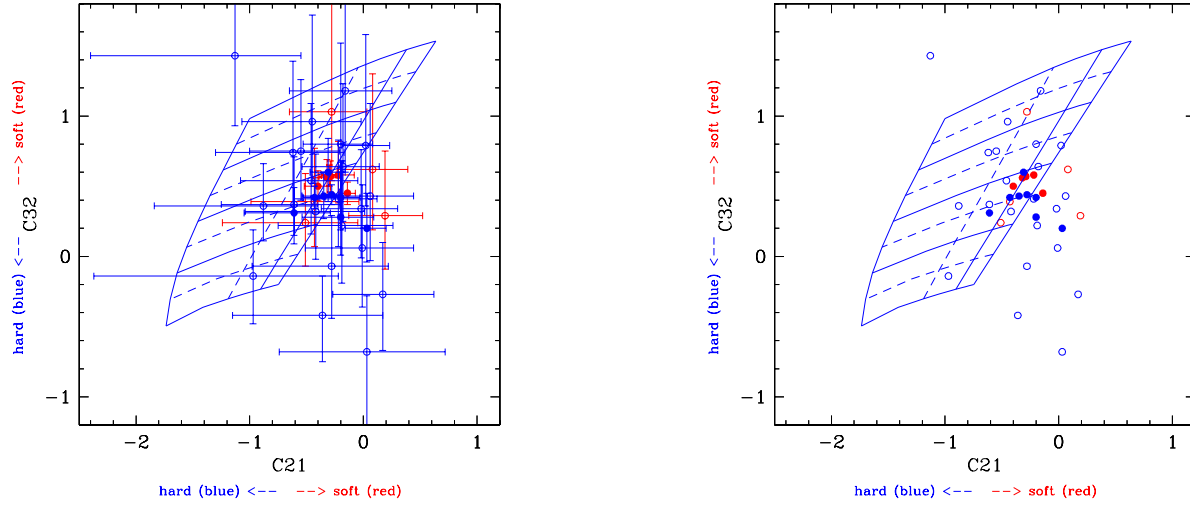


FIG. 2.— X-ray colors of point sources, left: with errorbars, and right: without errorbars (Sect. 3). The grid indicates photon index values of 0, 1, 2, 3, 4 (from bottom to top) and N_H values (from right to left) of 10^{20} , 10^{21} , 5×10^{21} (dashed one), 10^{22} cm^{-2} . Red circles correspond to sources at $R < 10''$, blue circles to sources between $R = 10''$ and the ellipse D25. Filled circles are sources with net counts > 30 , open circles with net counts < 30 .

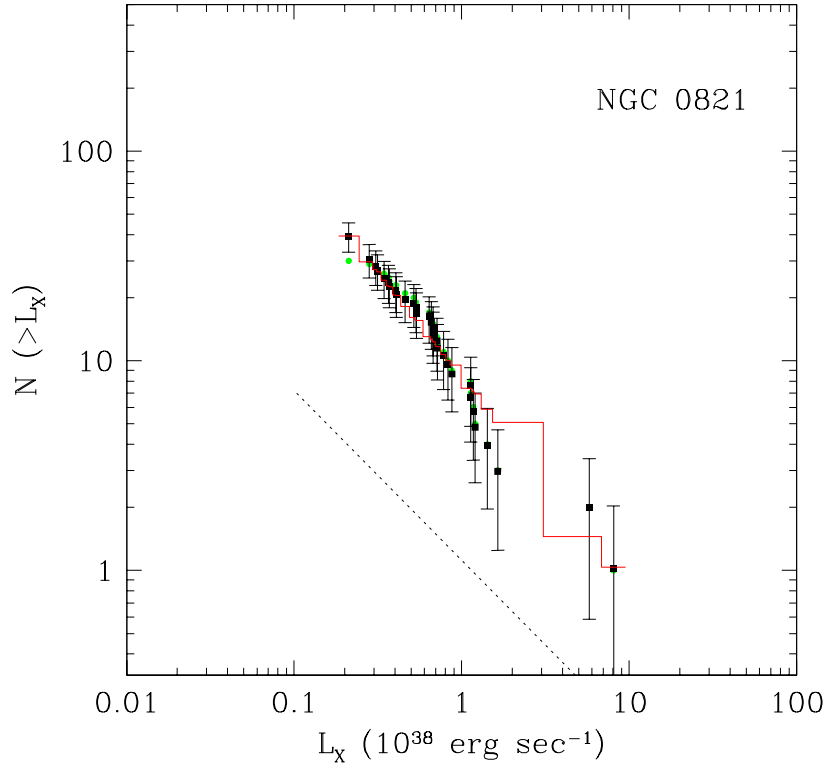


FIG. 3.— Cumulative XLF of point sources detected in the merged ACIS-S image within the D25 ellipse, with a central circle of $10''$ radius excluded (Sect. 3.1). Black squares with error bar show the bias-corrected function; green circles are the uncorrected function; the red histogram gives the best fit single power-law; the dotted line shows the expected number of cosmic X-ray background sources from the logN–logS relation of ChaMP plus CDF data (Kim, M. et al. 2006).

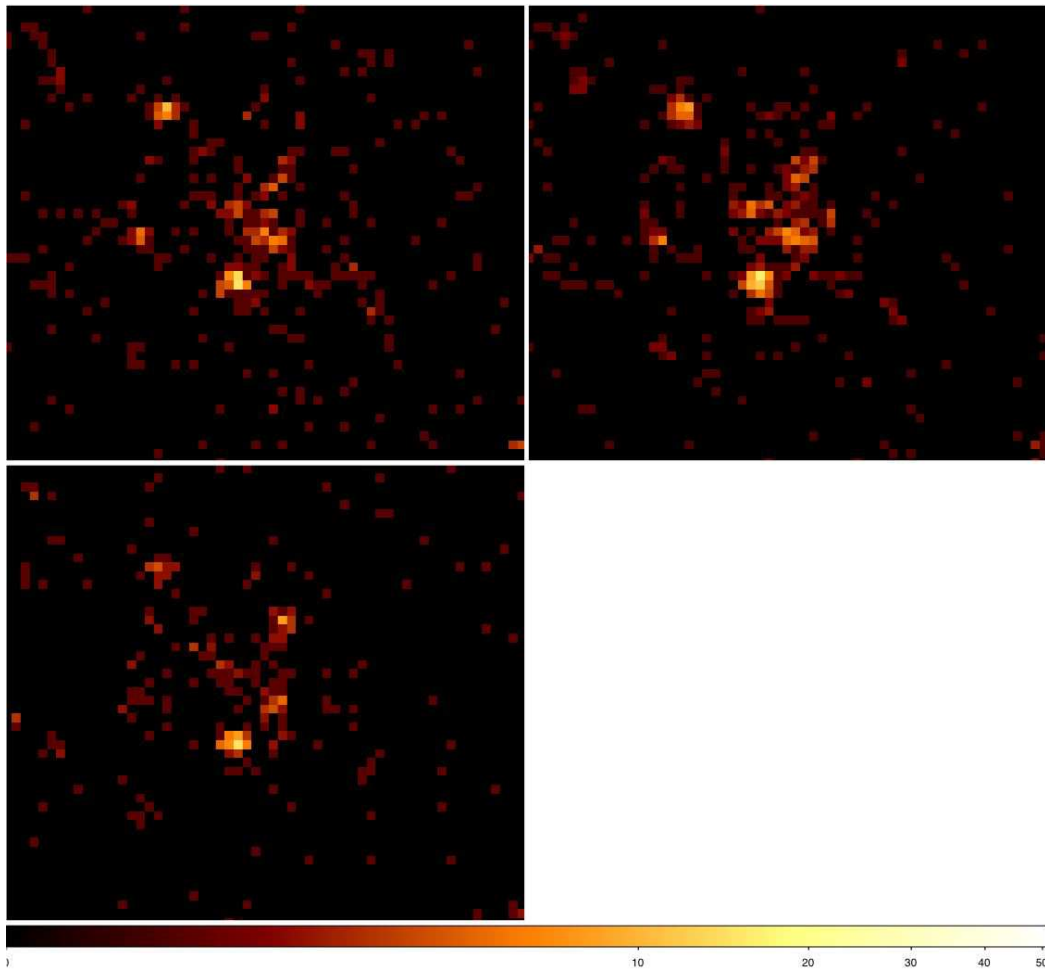


FIG. 4.— Co-added *Chandra* ACIS-S image of a central field of $25'' \times 25''$ in three bands: 0.3–1 keV (top left), 1–2 keV (top right), and 2–4 keV (bottom left). North is up and east is to the left. The bar below the figure gives the correspondence between the color scale and the number of counts/pixel (the size of 1 px is $0''.5$). See Sect. 4 for more details.

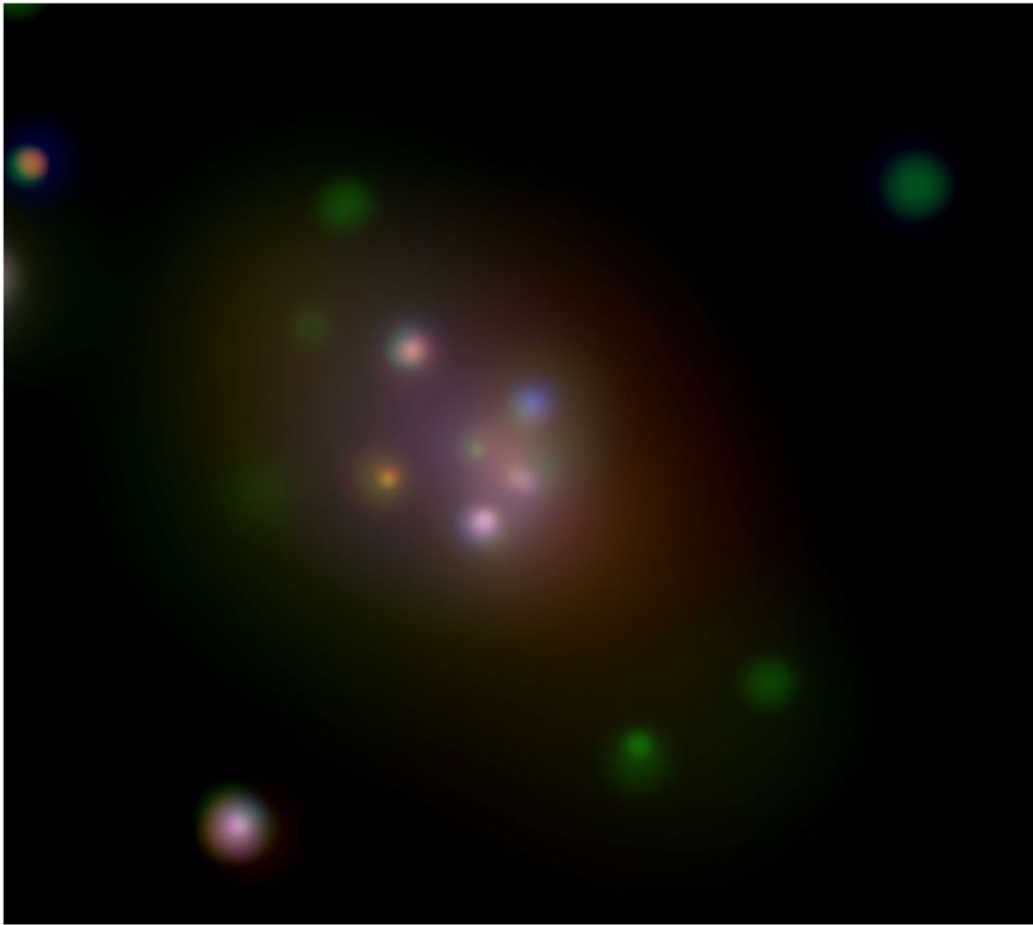


FIG. 5.— Co-added smoothed "true-color" image of a central $55'' \times 55''$ field (see details in Sect. 4). The red, green and blue colors correspond to the 0.3–1 keV, 1–2 keV and 2–4 keV bands respectively. North is up and east is to the left. The diffuse emission follows the optical shape of the galaxy (see Tab. 1, Fig. 1 and Fig. 7 below).

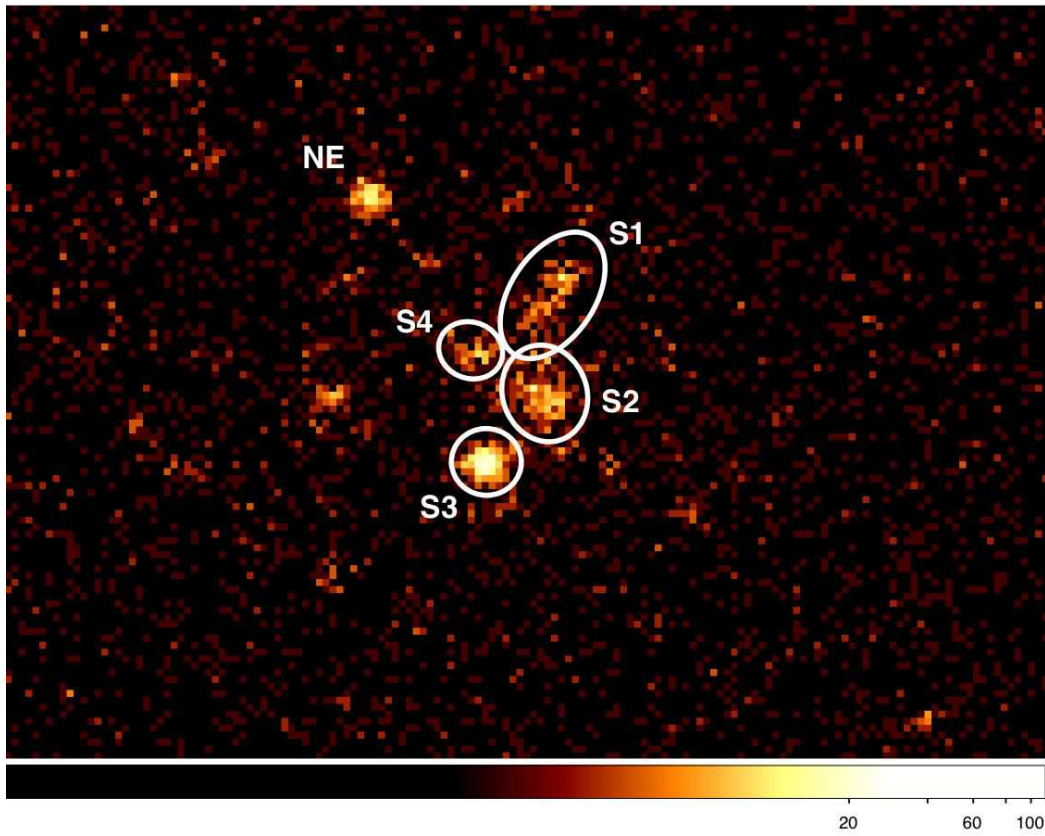


FIG. 6.— The ACIS-S image in the 0.3–6 keV band of the central $40'' \times 25''$ region of NGC 821, with the sources and their extent detected by the CIAO task *wavdetect* (Sect. 4.1). North is up and east is to the left. Here $1 \text{ px} = 0''.25$. The semi-major and semi-minor axes for S1–S4 are respectively $2''.5 \times 1''.5$, $1''.7 \times 1''.5$, $1''.2 \times 1''.2$ and $1''.2 \times 1''.0$.

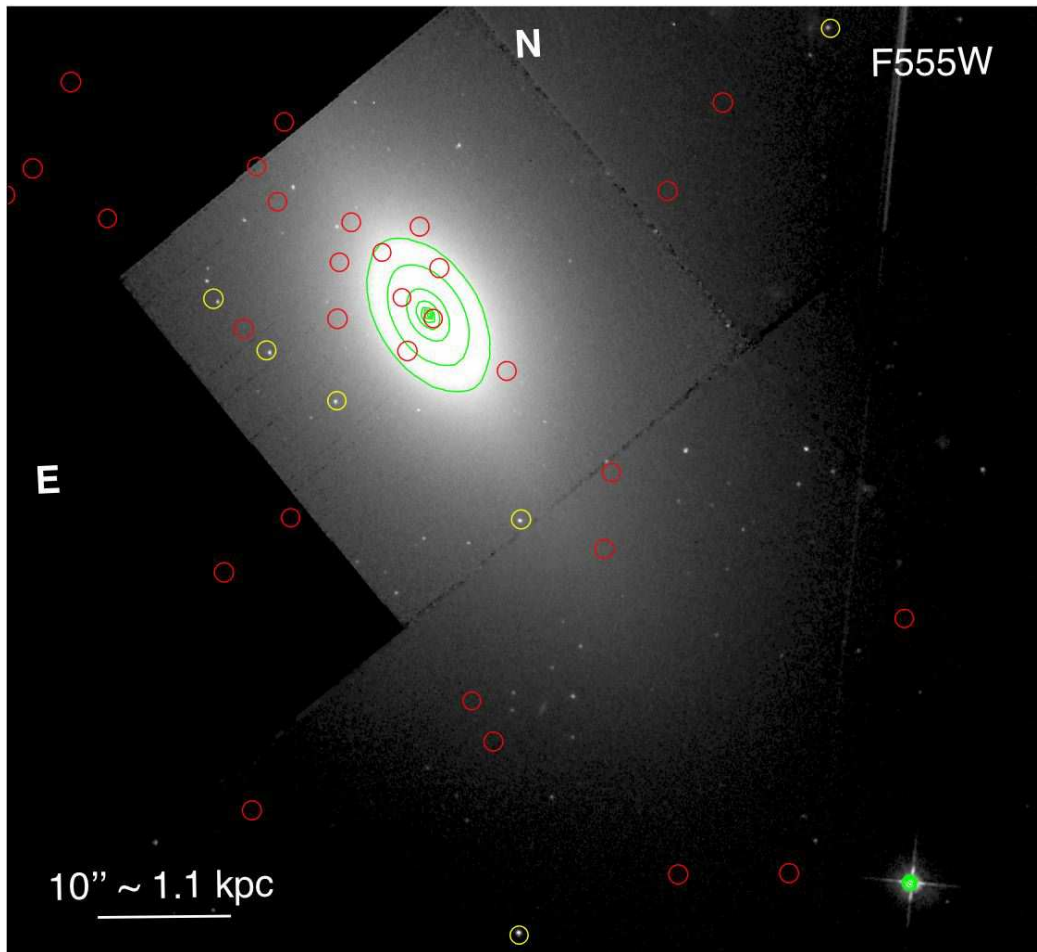


FIG. 7.— *HST* WFPC2 image of NGC821, with six *Chandra* ACIS-S sources falling within the D25 ellipse marked with yellow circles. *HST* isophotes in the central galactic region are also overlaid (see Sect. 4.2).

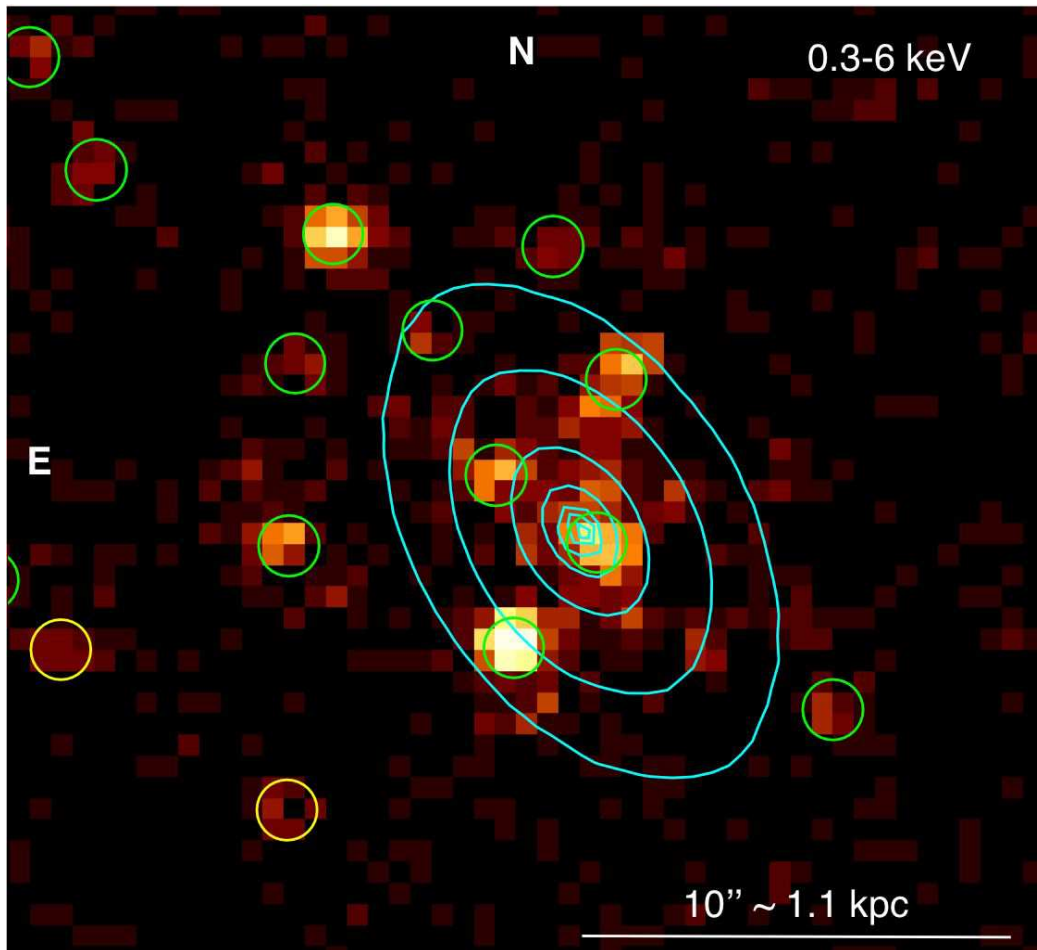


FIG. 8.— ACIS-S image of NGC821 with green circles of $0''.7$ radii marking the positions of the CIAO *wavdetect* sources ($1\text{px}=0''.5$), and yellow circles corresponding to globular clusters detected by *HST* (they are the same yellow sources of Fig. 7). The galactic isophotes are also overlaid; in the recalibrated WFPC2 image, they are centered at $\text{RA}=02^{\text{h}}\ 08^{\text{m}}\ 21^{\text{s}}.13$, $\text{Dec}=+10^{\circ}\ 59'\ 41''.8$ (see Sect. 4.2). The WFPC2 galactic center falls within the circle of the *Chandra* source S2.

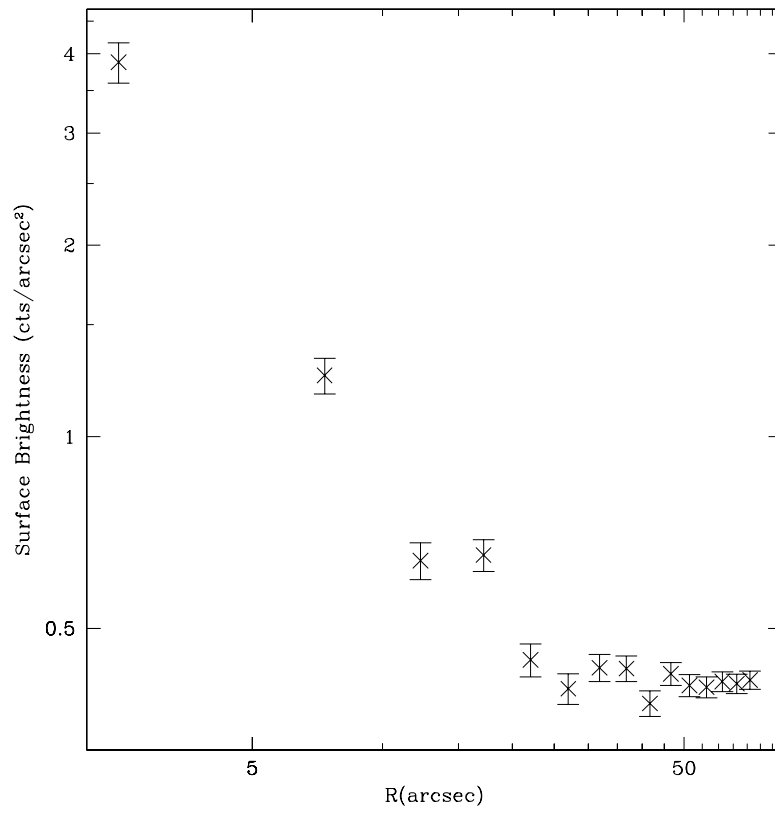


FIG. 9.— Radial profile of the (0.3–6 keV) emission, after removal of sources detected by *wavdetect* (Sect. 5.1). The flattening at radii $\gtrsim 25''$ is due to field background. Vertical bars give the $\pm 1\sigma$ uncertainty.

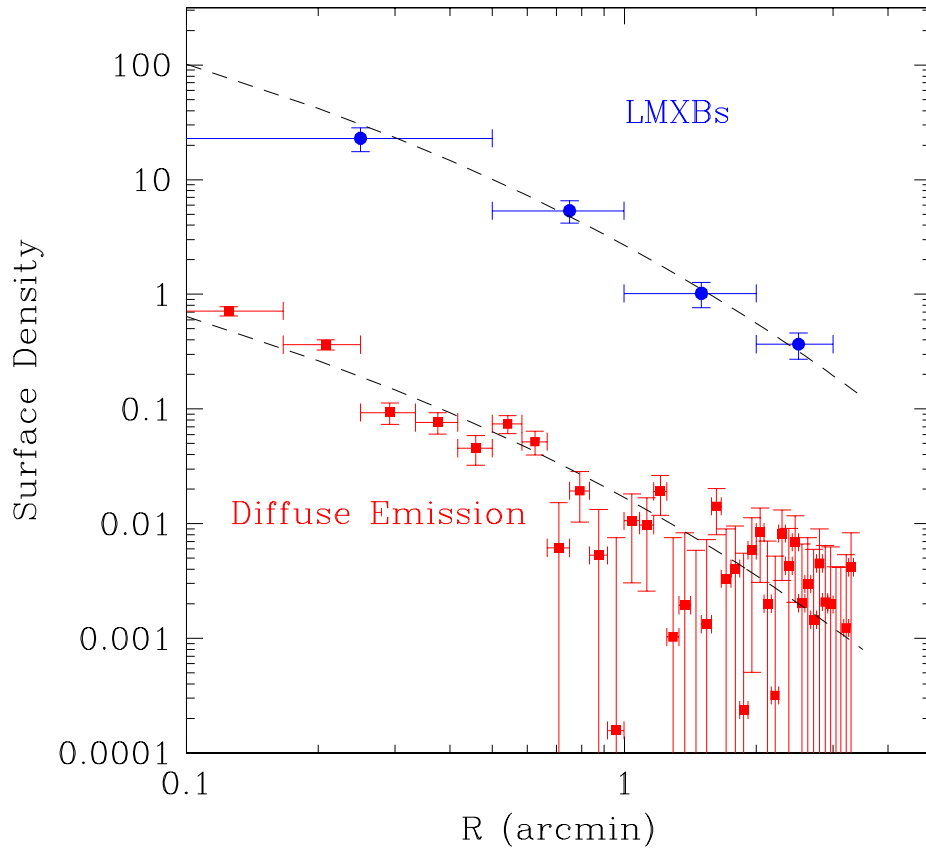


FIG. 10.— Radial profiles of: detected point sources (in blue), in units of number/square arcmin; background-subtracted diffuse emission over 0.3–6 keV (in red), in units of counts/pixel; galactic R-band emission (dashed lines, arbitrarily normalized). See Sect. 5.3 for details.

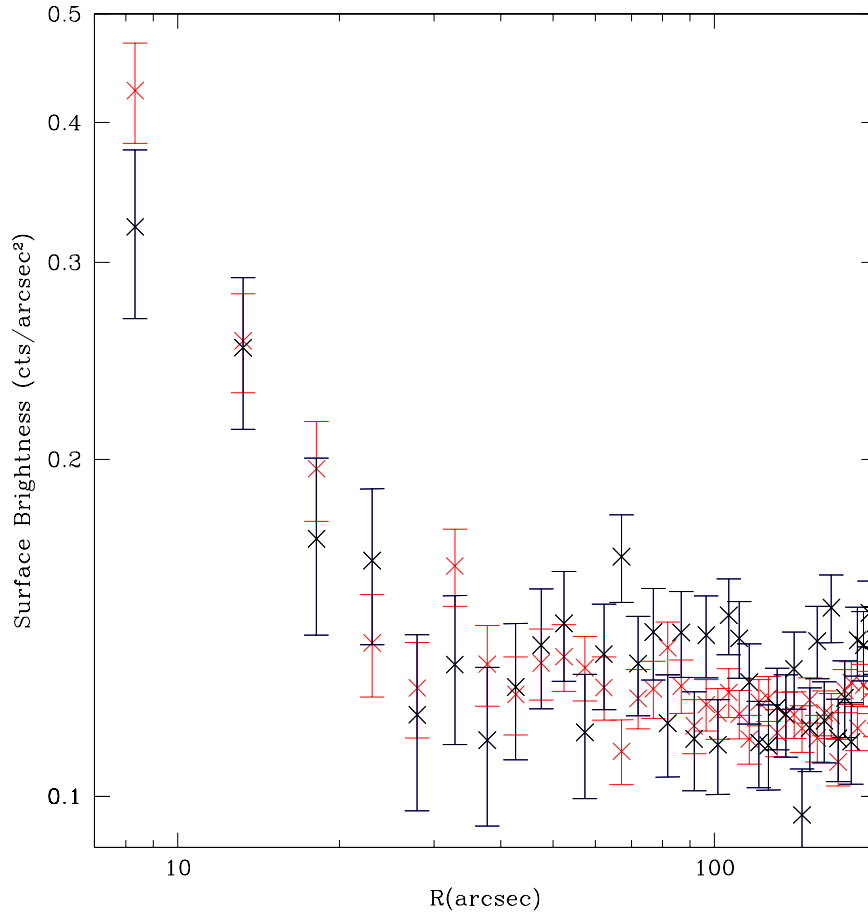


FIG. 11.— Radial distribution of the diffuse 0.3–1.5 keV emission (in black) that is implied by the observed 1.5–6 keV emission, when assuming for it the spectral model described in Sect. 5.4. In red the observed profile in the same 0.3–1.5 keV band is also shown. The flattening at large radii is due to field background. Vertical bars give the $\pm 1\sigma$ uncertainty.